INL/RPT-23-74848

Preliminary results addressing material qualification using combined ion irradiation and modeling data

September 2023

Andrea Jokisaari[1], Peter Baldo[2], Weiying Chen[2], Yiren Chen[2], Dzmitry Harbaruk[2], Josh Hlavenka[2], Sourabh Bhagwan Kadambi[1], Jia-hong Ke[1], and Mathew Swisher[1]

[1]*Idaho National Laboratory*
[1]*Argonne National Laboratory*

Idaho National Laboratory

INL is a U.S. Department of Energy National Laboratory operated by Battelle Energy Alliance, LLC

INL/RPT-23-74848

Preliminary results addressing material qualification using combined ion irradiation and modeling data

Andrea Jokisaari[1], Peter Baldo[2], Weiying Chen[2], Yiren Chen[2], Dzmitry Harbaruk[2], Josh Hlavenka[2], Sourabh Bhagwan Kadambi[1], Jia-hong Ke[1], and Mathew Swisher[1]

[1]Idaho National Laboratory
[1]Argonne National Laboratory

September 2023

Idaho National Laboratory
Idaho Falls, Idaho 83415

http://www.inl.gov

Prepared for the
U.S. Department of Energy
Office of Nuclear Energy
Under DOE Idaho Operations Office
Contract DE-AC07-05ID14517

Page intentionally left blank

SUMMARY

Additively-manufactured (AM) materials have attracted increasing attention in recent years as a new method to make novel and customized components. While AM and conventionally produced materials are compositionally similar, they do possess different microstructures, necessitating assessment of materials produced via AM for their behavior in reactor environments. Some microstructures unique to AM materials, such as compositional micro-inhomogeneity and dislocation cell structures, are of particular importance since they may lead to different radiation performance. The performance of AM materials for advanced nuclear reactor applications is of interest to the Advanced Materials and Manufacturing Technologies (AMMT) program under the Department of Energy Office of Nuclear Energy.

Ion irradiation is a critical tool for understanding the irradiation responses of AM materials. The range of conditions that materials will experience in advanced reactors, such as neutron spectrum, flux, and temperature, are much greater than that of traditional light water reactors. Combined with the incredible range of microstructures achievable with additive manufacturing, quantifying materials' radiation responses with only neutron irradiation is time- and cost-prohibitive. Ion irradiation can induce damage up to a few displacements per atom in hours with ions rather than in years with neutrons, enabling a much shorter irradiation-characterization cycle. Nonetheless, the high damage rate with ions can also have a profound impact on damage production and evolution, leading to different microstructures between the ion- and neutron-irradiated specimens.

To predict neutron irradiation performance of a new material on an accelerated time line, ion irradiation testing must be paired with modeling and simulation and a limited amount of neutron irradiation testing. Irradiation phenomena may be accelerated, altered, or even absent during ion irradiation and must be analyzed with modeling to utilize the ion irradiation results to predict material performance in reactor service. The ultimate goal is to use a combination of ion irradiation and modeling combined with a limited set of neutron irradiation results from test reactor conditions to predict the behavior of materials in a variety of prototypical advanced reactor conditions on an accelerated timeline.

The AMMT program aims to demonstrate its new accelerated development and qualification methods via laser powder bed fusion (LPBF) 316 stainless steel (SS). Focusing on material bearing both 316L and 316H specifications, we integrate ion irradiation and modeling. This year, we focus on answering foundational questions related to process variability, alloy chemistry variation,

and microchemical segregation. Experimental results provide information and motivate questions to the modeling effort, which aims to develop the ability to model radiation-driven microstructural evolution in additively-manufactured 316 stainless steel under a variety of advanced reactor conditions, including different temperatures, neutron spectra, and fluxes, in a sort of "virtual experiment". We perform *in-situ* and *ex-situ* ion irradiations and microstructural characterizations to support the development of AM materials for reactor applications, develop a phase field model of radiation-induced segregation in additively manufactured material with high angle grain boundaries and dislocation cells, and investigate the effect of carbon and chromium content on point defect behavior.

We find that processing conditions do not significantly impact the as-built microstructure or compositional micro-heterogeneity. We do find that AM microstructures have characteristic differences from conventional wrought material, including dispersed populations of nanoscale oxides and dislocation cells with microsegregation. We find that radiation-induced segregation behavior is much stronger for high-angle grain boundaries versus for the dislocation cell walls, and this difference is driven by the much higher sink strength and the much narrower width of a high angle grain boundary versus a dislocation cell wall. In addition, we find that temperature has a significant impact on the microstructure evolution; irradiation at 300 °C results in a large population of small, uniformly distributed dislocation loops that ultimately merge into network dislocations, while irradiation at 600 °C results in a smaller population of larger dislocation loops that form within the dislocation cells (that also eventually form network dislocations). Further characterization is required to quantify the effect of composition on microstructure evolution under irradiation at each temperature; however, atomistic studies indicate that any effect of carbon content on radiation damage behavior would likely arise not from direct alteration of collision cascade behavior but rather its impact on diffusive processes and properties. However, chromium content does appear to be directly proportional to the collision cascade size and the number of defects that survive the initial recombination phase, which may feed back into RIS behavior.

Further experimental characterization and modeling will shed light on the effect of temperature on radiation-driven microstructure evolution in additively manufactured materials and further explain the sensitivity of this microstructure evolution on process and compositional variability. This work positions the AMMT program strongly to integrate neutron irradiation data and to achieve the goal of using combined ion and neutron irradiation for accelerated qualification of materials for deployment in nuclear reactors.

ACKNOWLEDGEMENTS

The authors of this work would like to thank Stephen Taller and Rongjie Song for many useful discussions. This research made use of the resources of the High Performance Computing Center at Idaho National Laboratory, which is supported by the Office of Nuclear Energy of the U.S. Department of Energy and the Nuclear Science User Facilities under Contract No. DE-AC07-05ID14517. This work was sponsored by the U.S. Department of Energy, Office of Nuclear Energy, Advanced Materials and Manufacturing Technologies (AMMT) program. This manuscript has been authored in part by Battelle Energy Alliance, LLC under Contract No. DE-AC07-05ID14517 and by Argonne National Laboratory, managed and operated by UChicago Argonne LLC, under Contract No. DE-AC02-06CH11357.

Page intentionally left blank

CONTENTS

FIGURES

ACRONYMS

1D	one-dimensional
AM	additive manufacturing
AMMT	Advanced Materials and Manufacturing Technologies
ANL	Argonne National Laboratory
BCC	body centered cubic
CPU	Central processing unit
dpa	displacements per atom
EAM	embedded atom method
EDM	electrical discharge machine
FCC	face centered cubic
GB	grain boundary
GPU	Graphical processing unit
HAGB	high angle grain boundary
IVEM	Intermediate Voltage Electron Microscope
MD	molecular dynamics
MOOSE	Multiphysics Object-Oriented Simulation Environment
ORNL	Oak Ridge National Laboratory
PF	phase-field
PKA	primary knock-on atom
RIS	radiation-induced segregation
SIA	self-interstitial atoms
SS	stainless steel
TEM	transmission electron microscope
ZBL	Ziegler, Biersack, and Littmark

Page intentionally left blank

1. INTRODUCTION

The development of metal additive manufacturing (AM) has provided new opportunities to advancing material technologies. Components with limited fabrication runs and complex geometries can be manufactured rapidly and cost effectively with AM, leading to a wide range of material and design innovations. As such, AM materials have attracted increasing attention in recent years as a new method to make novel and customized components. While AM and conventionally produced materials are compositionally similar, they do possess different microstructures. Porosity, anisotropic grains, inclusions, dislocation cell structures, and microchemical inhomogeneity resulting from the printing process are often observed in AM materials. These microstructures and their behavior under service conditions must be evaluated carefully before AM materials can be widely adopted in the nuclear industry. The service performance of AM materials for nuclear applications is of interest to the Advanced Materials and Manufacturing Technologies (AMMT) program under the Department of Energy Office of Nuclear Energy (DOE NE) with the objective of accelerating the development of advanced materials and manufacturing technologies. The response of AM materials to irradiation in reactor service environments is crucial for the reliability and safety of nuclear reactor components. Every new material to be used in reactor environments must be assessed for its irradiation response, and AM materials are no exception. Some microstructures unique to AM materials, such as compositional micro-inhomogeneity and dislocation cell structure, are of particular importance since they may lead to different radiation performance.

Ion irradiation can be a critical tool for understanding the irradiation responses of AM materials. The range of conditions that materials will experience in advanced reactors, such as neutron spectrum, flux, and temperature, are much greater than that of traditional light water reactors. Combined with the incredible range of microstructures achievable with additive manufacturing, quantifying materials' radiation responses with only neutron irradiation is time- and cost-prohibitive. Compared with neutron irradiation, ion irradiation is more accessible, produces no or very low radioactivity, and radiation environments (e.g., temperature) can be much more carefully controlled. More importantly, ion irradiation in a typical beam line facility can cause much more rapid displacement damage than neutron irradiation in a test reactor, decreasing the time needed for achieving high damage levels. Specimens can be irradiated to a few displacements per atom (dpa) in hours with ions rather than in years with neutrons, enabling a much shorter irradiation-characterization cycle. Nonetheless, the high damage rate with ions can also have a profound impact on damage production and evolution, leading to different microstructures between the ion- and neutron-irradiated specimens.

Under irradiation, highly energetic particles cause collision and displacement cascades in structural stainless steel (SS) during which lattice atoms are knocked out of their positions. The radiation damage event can be classified into the collisional phase, which leads to the production of displaced atoms; the thermal spike phase, characterized by the collisional energy of the displaced atoms being spread across neighboring atoms; and the quenching phase, where

the majority of defects created in the previous phases migrate and recombine, leaving some population of defects including interstitials, vacancies, and defect clusters [1]. The relaxation phase may last from a few picoseconds to infinitely long times [1, 2]. While most of the generated point defects) recombine, the remaining point defects result in supersaturation beyond their thermal equilibrium concentrations. Those defects eventually diffuse, migrate, and aggregate to form larger defect clusters, such as stacking fault tetrahedra, interstitial clusters, dislocation loops, and voids [3, 4]. However, at extended defects such as grain boundary (GB)s and dislocation cell walls (in cold-worked or AM microstructures), point defects can be absorbed or annihilated, resulting in local concentrations closer to equilibrium. Therefore, point defect fluxes and concentration gradients are established near GBs and cell walls. This influences atomic fluxes and concentration gradients since diffusion of atomic components is coupled to point defect migration. While atoms diffuse along the direction of self-interstitial atoms (SIA) via dumbbell motion, they generally diffuse in a direction opposite to that of vacancies via the vacancy-atom exchange mechanism. More importantly, for a given diffusion mechanism, each atomic component diffuses at a different rate. Over time, the sustained flux of point defects towards the sink and the associated diffusion of atomic components with different diffusivities results in atomic redistribution or radiation-induced segregation (RIS). The evolution of the microstructure due to radiation damage can cause serious deterioration of material properties, including radiation embrittlement, void swelling, hardening, creep, and eventually the failure of the material system [1]. Changes in chemical microsegregation can also affect the corrosion performance by altering the local chemical potential and stability of any protective (passivating) film.

To predict neutron irradiation performance of a new material on an accelerated time line, ion irradiation testing must be paired with modeling and simulation and a limited amount of neutron irradiation testing. Irradiation phenomena may be accelerated, altered, or even absent in ion irradiations and must be analyzed with modeling to utilize the ion irradiation results for prediction of the material's performance in reactor service. The ultimate goal is to use a combination of ion irradiation and modeling combined with a limited set of neutron irradiation results from test reactor conditions to predict the behavior of materials in a variety of prototypical advanced reactor conditions.

The AMMT program aims to demonstrate its new accelerated development and qualification methods via laser powder bed fusion (LPBF) 316 SS. Thus, we focus on LPBF 316 SS (both 316L and 316H compositions) for study and analysis. We integrate the ion irradiation results to guide our modeling investigation and provide feedback for experimental studies as part of our effort to understand the impact of microstructure and microchemical variability on radiation-driven microstructure evolution. We perform *in-situ* and *ex-situ* ion irradiations and microstructural characterizations to support the development of AM materials for reactor applications, allowing us to quickly explore the irradiation responses of different AM materials to identify the influential factors contributing to the performance of AM materials under irradiation and to provide

high-fidelity data in support of the development of irradiation damage models for AM materials. We lay the foundation of accurate predictions of microstructure evolution with a novel mesoscale phase-field (PF) model using the Multiphysics Object-Oriented Simulation Environment (MOOSE) framework [5–7] to study defect migration and RIS in the unique dislocation cell structure present in AM 316 SS. To inform mesoscale simulations, we perform atomistic studies with molecular dynamics. We predict the partial diffusivity of vacancies and interstitial atoms in 316 stainless steel at a range of temperatures, which underpins the mesoscale phenomenon of radiation-induced segregation. We also examine the effect of carbon and chromium on collision cascade behavior to shed light on whether they impact radiation-driven microstructure evolution from the initial damage event.

2. Experimental investigations

The experimental effort focuses on AM 316L and 316H SS specimens printed via laser power bed fusion. AM 316L SS is one of the most popular materials being produced with LPBF and some preliminary irradiation data are available in literature [8–11]. Conversely, AM 316H SS is relatively new and no prior study on its irradiation performance exists to our knowledge. The experimental data collected in this study can be compared with wrought 316 SS data in the literature to understand the difference between AM and wrought 316 SS. This section discusses the experimental method, including the material fabrication, preparation of *in-situ* and *ex-situ* irradiation specimens, irradiation experiments, microstructural examinations, and nanoindentation tests.

2.1 Materials and specimen preparation

Three AM builds were investigated in this study, designated as LPBF 316L-1, LPBF 316L-2, and LPBF 316H, with their compositions given in Table 1. These AM prints were produced via LPBF at two laboratories: the LPBF 316L-1 specimen was printed at Oak Ridge National Laboratory (ORNL) in the form of plates using a Concept Laser M2 system by GE. The same build was also neutron-irradiated and tested at ORNL [9]. The LPBF 316L-2 and LPBF 316H prints were produced at Argonne National Laboratory (ANL) in the form of small rectangular blocks using a Renishaw AM400 system. The printing parameters of these materials can be found in previous reports [12]. The composition of LPBF 316L-1 shown in Table 1 is the nominal composition of the powder provided by the vendor. The compositions of LPBF 316L-2 and LPBF 316H were measured by cutting a small piece from the build and analyzed with combustion infrared detection for carbon, inert gas fusion for hydrogen, oxygen and nitrogen, and direct current plasma emission spectroscopy for other elements.

The printed materials were machined into 3-mm-diameter rods with an electrical discharge machine (EDM) along their build directions. The rods were then cut into 550 μm-thick disks with EDM. For *in-situ* ion irradiations, the disks were mechanically polished on both sides with sandpaper to a thickness of approximately 100 μm, and then electropolished between -30 °C and -40 °C until perforation. The electrolyte used was composed of 5% perchloric acid and 95% methanol. For *ex-situ* ion irradiations, only one side of each disk was polished. The polishing was performed with sandpaper to P4000 grit, polycrystalline diamond suspension to 1 μm, vibratory polishing using 50 nm colloidal silica polishing suspension, and finally electropolishing at -30 °C to -40 °C using the same electrolyte for 20-30 seconds.

2.2 *In-situ* and *ex-situ* ion irradiations

In-situ ion irradiations were performed in the Intermediate Voltage Electron Microscope (IVEM)-Tandem Facility at ANL using a NEC implanter and a Hitachi-9000 TEM [13]. A Gatan double-tilt heating holder was used. The irradiation parameters are given in Table 2. For each

Table 1: Composition (wt%) of the LPBF 316 stainless steels assessed

	Build identifier		
Element	LPBF 316L-1	LPBF 316L-2	LPBF 316H
Oxygen	0.05	0.037	0.046
Nitrogen	0.01	0.095	0.015
Carbon	0.006	0.017	0.04
Sulfur	-	0.009	0.005
Iron	Bal.	Bal.	Bal.
Chromium	17.1	16.55	17.04
Manganese	1.19	0.57	1.09
Silicon	0.46	0.59	0.45
Nickel	12.1	12.33	12.22
Copper	0.01	0.12	0.007
Molybdenum	2.41	2.26	2.57
Vanadium	-	0.057	0.01
Phosphorus	<0.005	0.013	0.018
Cobalt	0.1	0.058	0.028
Tungsten	-	<0.002	<0.002

Table 2: Irradiation parameters of *in-situ* ion irradiation

Build Identifier	Ion	Temperature (°C)	Dose Rate (dpa/s)	End Dose (dpa)
LPBF 316L-1	1 MeV Kr^{2+}	300	10^{-3}	5
		600		
LPBF 316L-2		300		
		600		
LPBF 316H		300		
		600		

in-situ irradiation experiment, bright-field (BF) mages, dark-field (DF) images and diffraction patterns were taken at 0.3 dpa, 0.6 dpa, 1 dpa, 3 dpa and 5 dpa to show the defect evolution as a function of dose. The vacuum of the TEM chamber was maintained below 3×10^{-7} torr throughout the in-situ irradiation experiments.

Ex-situ ion irradiations were performed with a tandem accelerator. The irradiation parameters are given in Table 3. The specimens were heated with an electric filament, and a thermocouple was attached to the specimen holder for temperature control. The vacuum of specimen chamber was maintained on the order of 10^{-7} torr during irradiation.

2.3 Post-irradiation examination

The as-printed LPBF 316H and LPBF 316H *in-situ* irradiated at 600 °C were examined with EDS mapping on a Thermal Fisher Talos transmission electron microscope (TEM) in the Center for Nanoscale Materials at Argonne National Laboratory, with a focus on the dislocation cell structures, grain boundaries, and precipitates. Nanoindentation using a Bruker TI Premier was performed on as-printed and *ex-situ* irradiated specimens. The load pattern used 5 seconds to ramp the load, 2 seconds to hold the load, and 5 seconds to ramp down the load. For each specimen, 100 indents were performed under load control. Using these conditions, hardness for a contact depth ranging from approximately 100 nm to 220 nm was accessed.

2.4 Results of TEM examinations of as-printed microstructures

Figure 1 presents the TEM results obtained from the as-printed LPBF 316L-1 SS. Figures 1a and 1b show the dislocation cell structure resulting from the printing process. The average size of the cells, as measured from the short axis of the elliptical-shaped cells, is 505 ± 38 nm. Figure 1c shows the diffraction pattern taken under a two-beam condition near the $\langle 001 \rangle$ zone axis. Figure 1d and Figure 1e are the magnified under-focused BF images showing small particles decorating the dislocation cell walls. Their average size is 18.5 nm, but some of the largest particles are almost 100 nm, as shown in the size distribution plot in Figure 1f. These particles are reported as (Si, Mn) oxides previously in the literature [9, 10]. Besides the silicon oxides, large inclusions with a size of

Table 3: Irradiation parameters of *ex-situ* ion irradiation

Build Identifier	Ion	Temperature (°C)	Dose Rate (dpa/s)	Dose (dpa)	Nanoindentation
LPBF 316L-1	4 MeV Ni^{2+}	300	10^{-3}	0.2	
				2	
				5	
				10	
			10^{-4}	0.2	
				2	
			10^{-5}	0.2	
		600	10^{-3}	0.2	yes
				2	yes
				5	yes
				10	yes
			10^{-4}	0.2	
				2	
			10^{-5}	0.2	

1-2 μm were observed occasionally in the TEM foil as shown in Figure 1g. The corresponding EDS spectrum in Figure 1h indicates that the inclusion contains Mn, Cr, Si, Al, and O. The tantalum signal is from the specimen holder.

Figure 2 shows the TEM analysis of as-printed LPBF 316L-2. Figure 2a shows the dislocation cell structure, where the average cell size is 509 ± 51 nm. Figures 2b and 2c show the BF and DF images of a dislocation cell. Figure 3 shows the TEM analysis of as-received LPBF 316H. Figure 3a is the low-magnification BF image showing the dislocation cell structures in the as-printed LPBF 316H SS. The cell size is 531 ± 75 nm. Similar to LPBF 316L-1, silicon oxides were observed decorating the dislocation cell walls in LPBF 316L-2 and LPBF 316H. Inclusions like those in LPBF 316L-1 were also observed in LPBF 316L-2 and LPBF 316H.

The elemental maps of as-printed LPBF 316H are shown in Figure 4. The dislocation cell wall is enriched in Cr, Mo and, marginally, Si, while Fe is depleted at the cell wall. The nanoparticles decorating the dislocation cell wall are enriched in Si, Mn, and O, and no carbides are observed. The elemental distribution observed in LPBF 316H is consistent with that of LPBF 316L reported previously [10, 14]. Overall, the as-printed LPBF 316L-1, LPBF 316L-2, and LPBF 316H show similar microstructures, featuring dislocation cells in the order of 500 nm, small silicon oxide nanoparticles decorating the cell walls, and chemical inhomogeneity primarily along the cell walls.

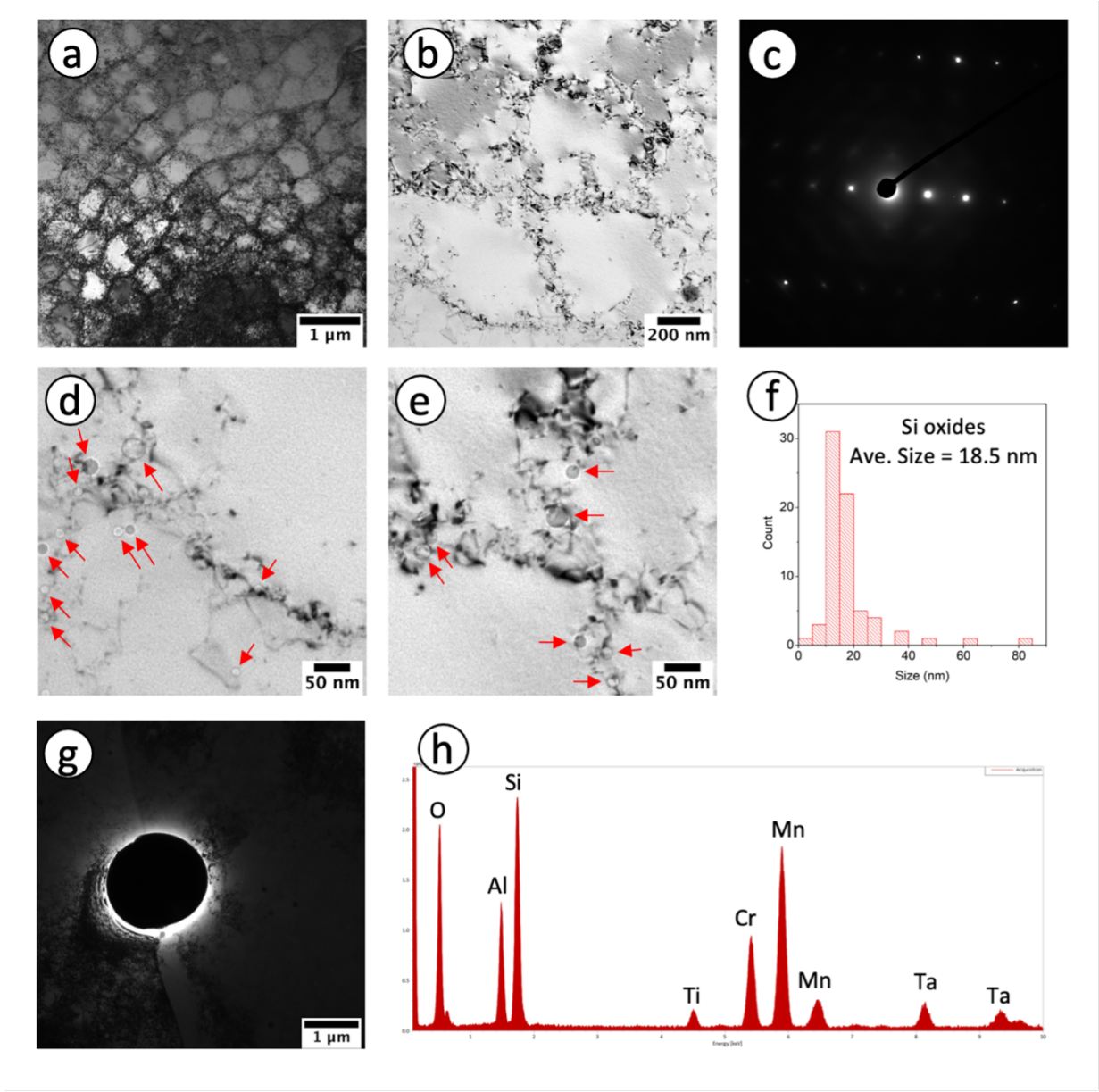

Figure 1: TEM results of as-printed LPBF 316L-1: (a) low-magnification BF TEM image. (b) high-magnification BF TEM image. (c) diffraction pattern taken at a two-beam condition of $\mathbf{g} = 200$ near the $\langle 001 \rangle$ zone axis. (d)(e) under-focused TEM images with a defocus of 5 μm. The red arrows indicate the oxide particles. (f) the size distribution of the oxide particles. (g) TEM image of an inclusion. (h) EDS spectrum of the inclusion.

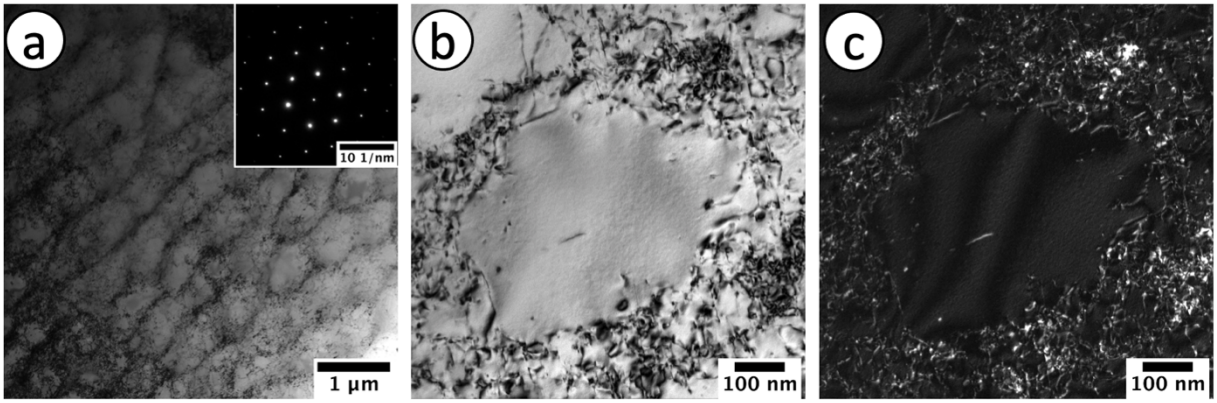

Figure 2: TEM images of as-printed LPBF 316L-2: (a) low-magnification BF TEM image. The inset is the diffraction pattern taken at the ⟨011⟩ zone axis. (b) BF TEM image of a dislocation cell. (c) the corresponding DF TEM image of the dislocation cell. The imaging condition for (b) and (c) is a two-beam condition with **g** = 200 near the ⟨011⟩ zone axis.

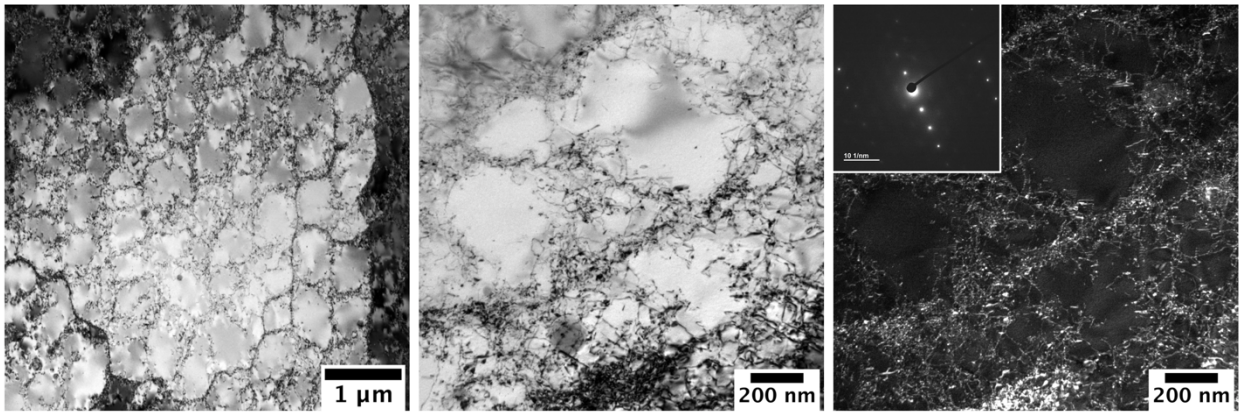

Figure 3: TEM images of as-printed LPBF 316H SS: (a) Low-magnification BF TEM image. (b) and (c) Higher-magnification BF and DF TEM images of a dislocation cell. The inset is the corresponding diffraction condition for the images (**g** = 200 near the ⟨011⟩ zone axis).

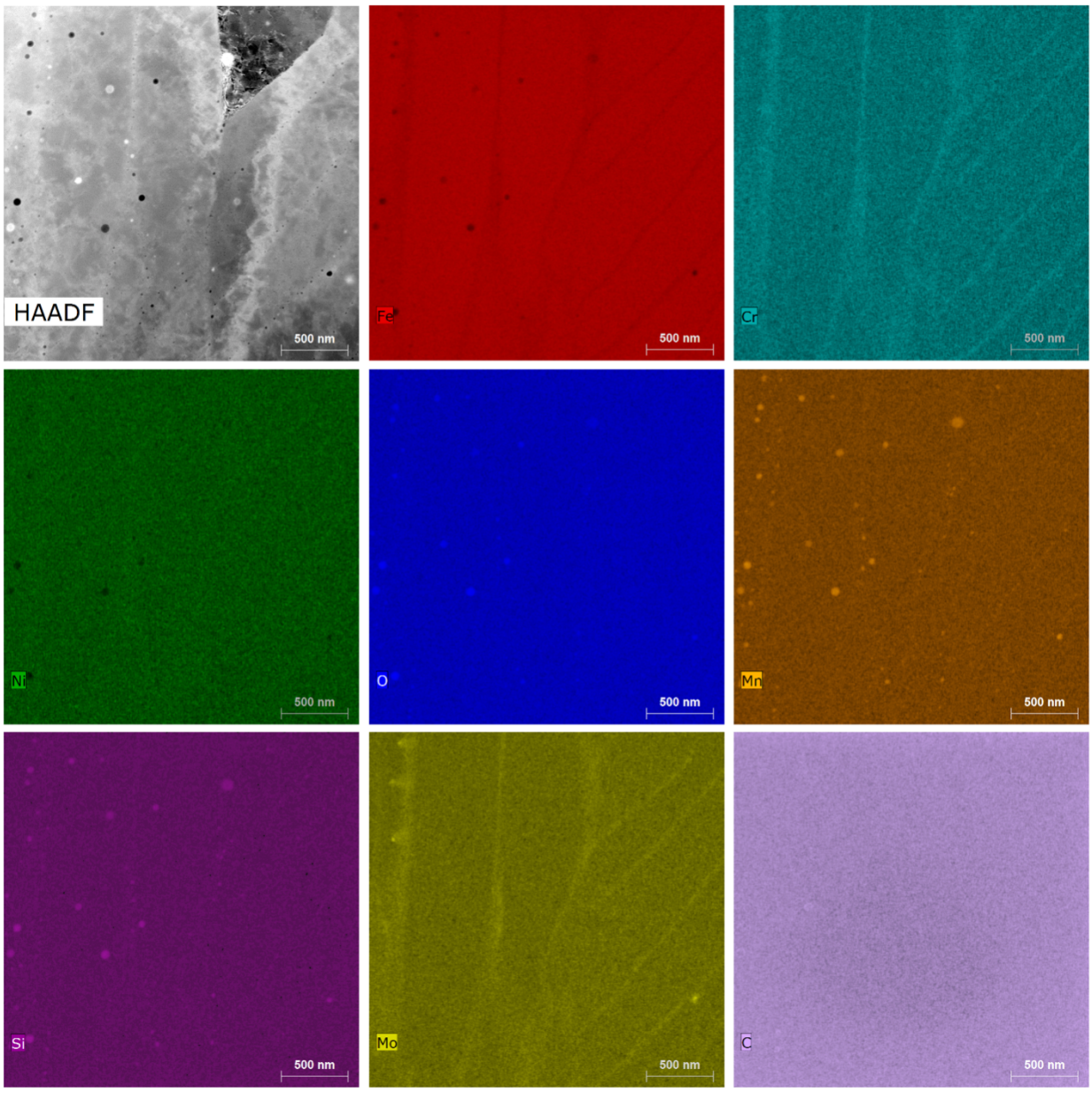

Figure 4: EDS composition maps of as-printed LPBF 316H.

2.5 Defect evolution under *in-situ* ion irradiation

2.5.1 Defect evolution in LPBF 316H SS

The microstructure of LPBF 316H SS continuously evolved under *in-situ* ion irradiation. Figure 5 and Figure 6 are two sets of TEM images taken during the 600 °C and 300 °C in-situ irradiations, respectively. For the irradiation at 600 °C, the irradiation-induced dislocation loops formed first near the center of the dislocation cells, which was defect-free prior to the irradiation. The preexisting cell walls tend to become narrower under irradiation, but no dislocation loops can be resolved inside the cell walls. The different responses to irradiation between the cell interior and cell walls indicate an effect of the dislocation cell structure on the loop formation. Both $\frac{1}{3}\langle 111\rangle$ faulted loops and $\frac{1}{2}\langle 110\rangle$ perfect loops were observed at 600 °C, and there was no obvious difference between the two types of dislocation loops in their location relative to the cell structure. With increasing irradiation dose, the loop size increased and more loops formed, occupying the previously loop-free area within the as-printed cell structure. At 3 dpa (Figure 5d), irradiation-induced dislocation loops occupied the entire cell interior. As the loop density and size increased, the frequency of the loop-loop interaction increased and eventually led to the formation of a dislocation network, as observed at 5 dpa (Figure 5e). The as-printed heterogeneous dislocation cell structure was replaced by a uniform dislocation network at damage greater than 5 dpa, and the prior cell walls were barely visible at high doses. It should be noted that, however, the observed defect evolution as a function of dose can be affected by foil thickness. At a different foil thickness, the exact doses for the different stages of the evolution may be different, although the general trend of defect evolution should remain the same.

In contrast to the results of 600 °C irradiation, the formation of irradiation-induced dislocation loops was less affected by the dislocation cell structure in the 300 °C irradiation. As shown in Figure 6a, even at the lowest dose of 0.3 dpa, a high density of dislocation loops was observed to be uniformly distributed within the preexisting dislocation cells. The dislocation walls became less organized under irradiation and quickly vanished with increasing dose. Up to 1 dpa, the majority of the irradiation-induced dislocation loops were small and difficult to characterize for their Burgers vectors. However, as shown in Figure 6f, some of the irradiation-induced dislocation loops can be determined as $\frac{1}{3}\langle 111\rangle$ faulted loops based on their edge-on appearance under the corresponding crystallographic orientation. With increasing irradiation dose, extended defects, such as large dislocation loops and dislocation segments, were observed at 3 and 5 dpa, and the density of dislocation loops decreased, which indicates the coalescence between irradiation-induced dislocation loops at high doses. No voids were observed at either irradiation temperature.

2.5.2 Defect evolution in LPBF 316L SS

Similar to LPBF 316H SS, the microstructure of LPBF 316L SS evolved with increasing dose under *in-situ* ion irradiations performed at 600 °C and 300 °C. The observations made in these *in-situ* experiments were consistent with a previous study reported on a different LPBF 316H build

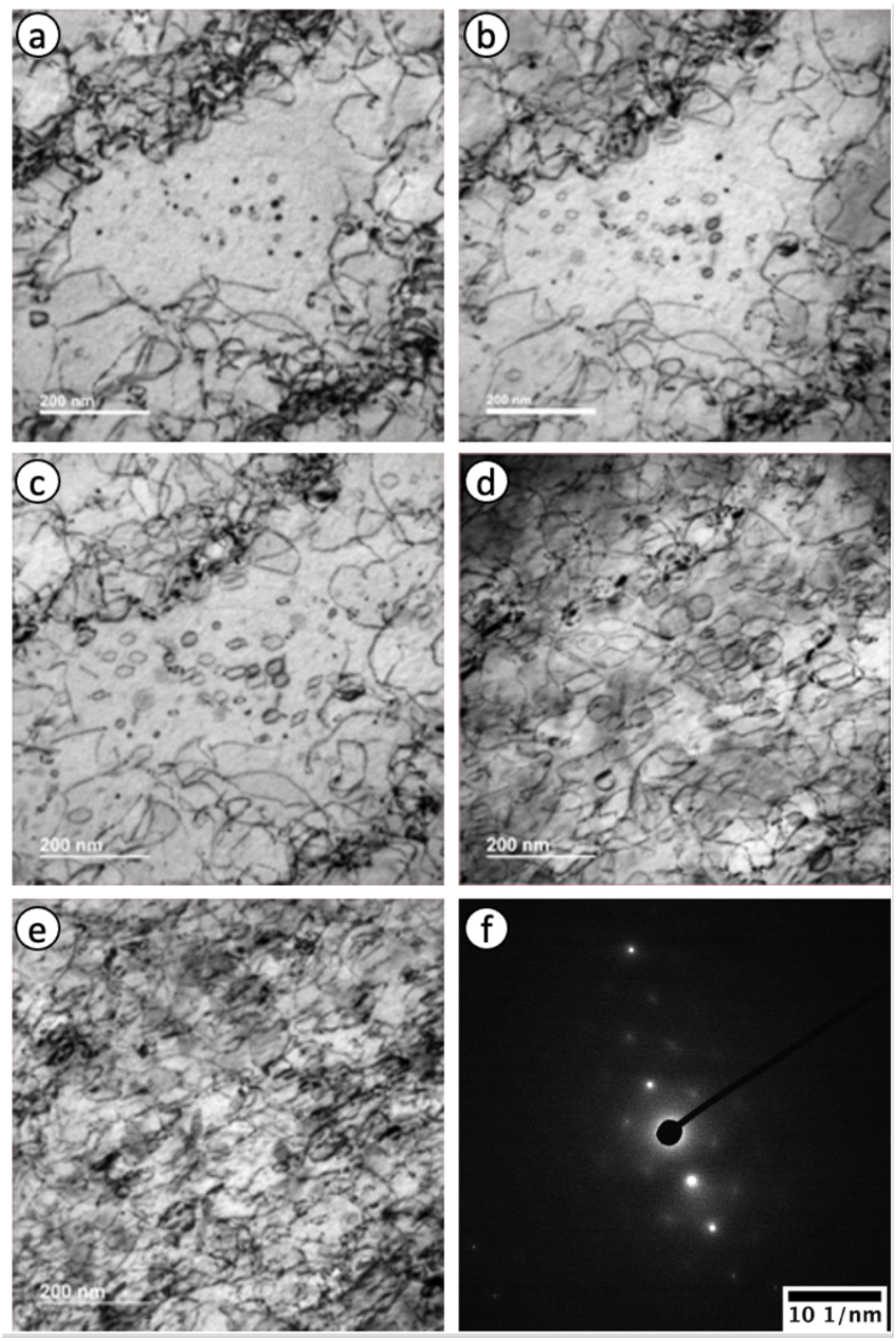

Figure 5: A set of same area BF TEM images of LPBF 316H in-situ irradiated with 1 MeV Kr ions at 600 °C to (a) 0.3 dpa, (b) 0.6 dpa, (c) 1 dpa, (d) 3 dpa and (e) 5 dpa. (f) The corresponding diffraction pattern of the two-beam condition (**g** = 200 near the ⟨011⟩ zone axis) used for the set.

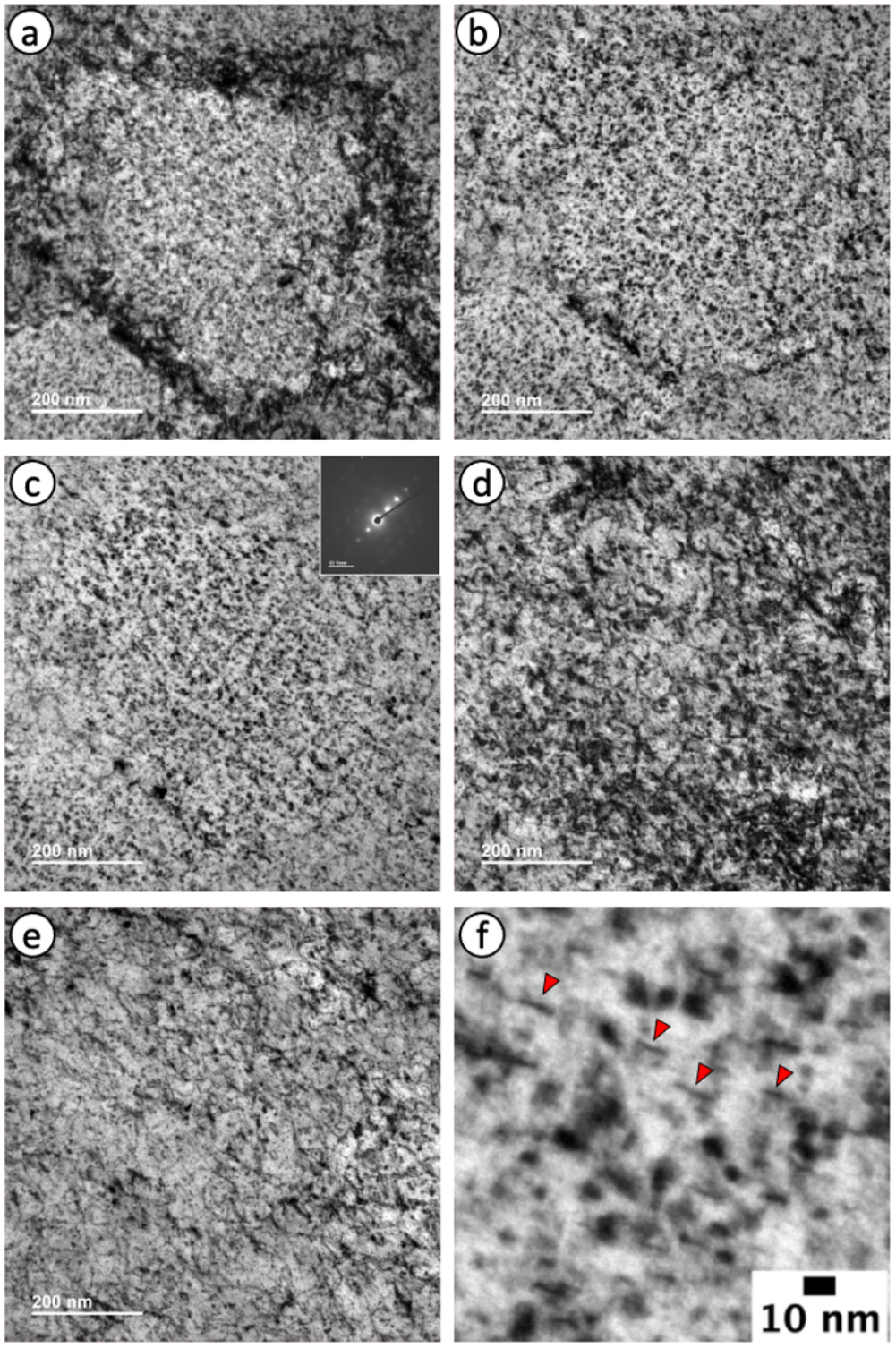

Figure 6: A set of same area BF TEM images of LPBF 316H in-situ irradiated with 1 MeV Kr ions at 300 °C to (a) 0.3 dpa, (b) 0.6 dpa, (c) 1 dpa, (d) 3 dpa and (e) 5 dpa. The inset is the diffraction pattern indicating the two-beam condition of $\mathbf{g} = 200$ near the $\langle 011 \rangle$ zone axis. (f) A high-magnification image of the 1 dpa sample. The red arrows indicate the edge-on faulted dislocation loops.

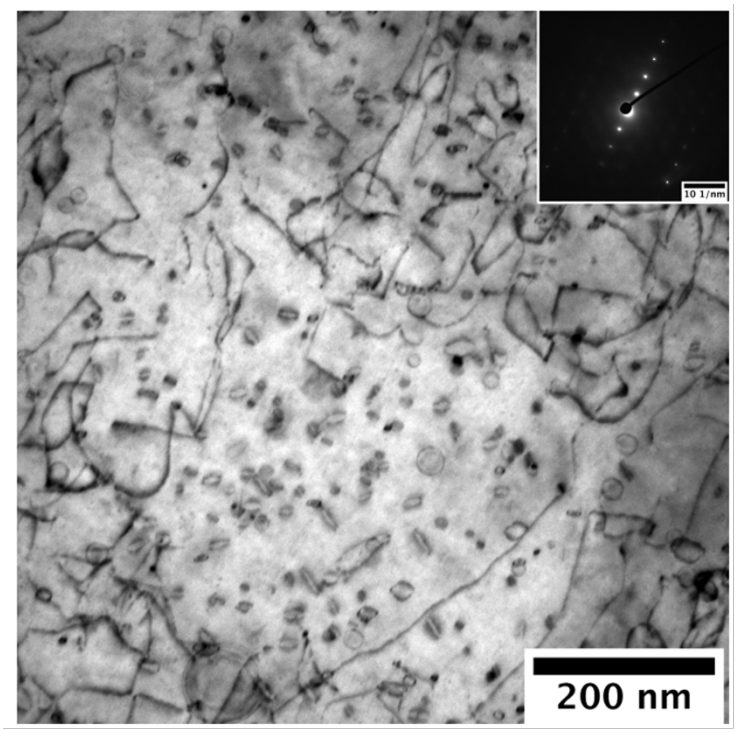

Figure 7: BF TEM image of LPBF 316L-1 *in-situ* irradiated with 1 MeV Kr ions at 600 °C to 1 dpa. The inset is the imaging condition – a two-beam condition with g = $11\bar{1}$ near the $\langle 011 \rangle$ zone axis.

[10]. Figure 7 and Figure 8 show the TEM images of LPBF 316L-1 and LPBF 316L-2, respectively, irradiated at 600 °C to 1 dpa. Like the LPBF 316H, large $\frac{1}{3}\langle 111 \rangle$ faulted loops and $\frac{1}{2}\langle 110 \rangle$ perfect loops were produced by irradiation preferentially at the interior of dislocation cells. Figure 9 and Figure 10 show the TEM images of LPBF 316L-1 and LPBF 316L-2, respectively, irradiated at 300 °C to 1 dpa. Again, a high density of small dislocation loops was observed uniformly within the cell structure. The loop size and density were different among LPBF 316L-1, LPBF 316L-2, and LPBF 316H, making it possible to study the effect of composition (e.g. carbon content differences between 316L vs 316H) on irradiation damage. However, because TEM foil surfaces are defect sinks that could strongly affect the defect evolution [15, 16], a careful analysis of foil thickness is essential to make quantitative comparisons among different samples.

2.5.3 RIS in LPBF 316H SS

Figure 11 shows the elemental maps of LPBF 316H *in-situ* irradiated at 600 °C to 5 dpa. Irradiation-induced segregation (RIS) at grain boundaries was observed. Cr and Mn were depleted, while Si, Ni and some trace amounts of O were enriched. No carbides were observed after irradiation. Instead, a high density of small Cr-rich oxide rods with a length of 50-100 nm and a width of 10-20 nm were observed. The presence of such a high density of nanoparticles can have an impact on mechanical properties and therefore merit further investigation. To address whether irradiation induced the Cr-rich oxide formation or whether it is purely a thermal effect, a

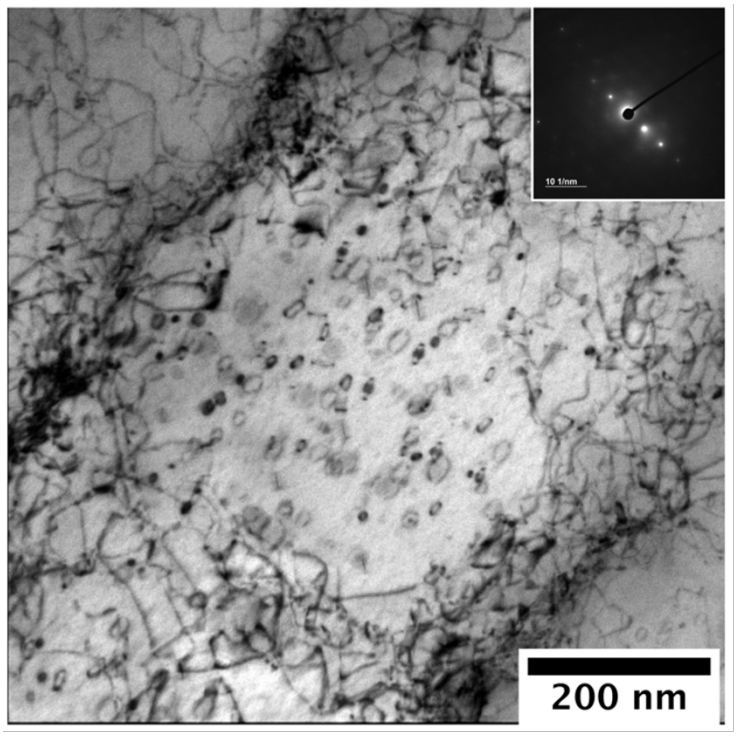

Figure 8: BF TEM image of LPBF 316L-2 in-situ irradiated with 1 MeV Kr ions at 600°C to 1 dpa. The inset diffraction pattern is the imaging condition – a two-beam condition with $\mathbf{g} = 200$ near the $\langle 011 \rangle$ zone axis.

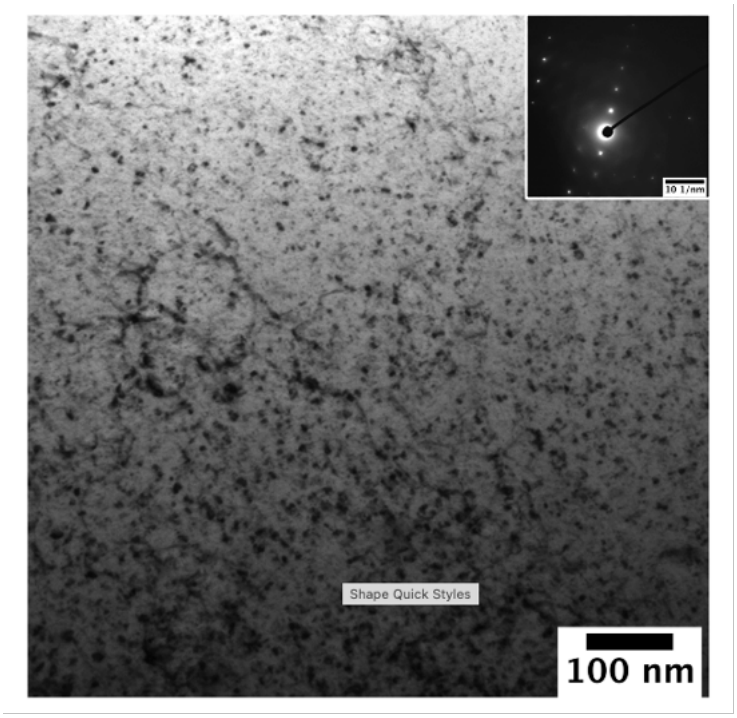

Figure 9: BF TEM image of LPBF 316L-1 in-situ irradiated with 1 MeV Kr ions at 300°C to 1 dpa. The inset diffraction pattern is the imaging condition – a two-beam condition with **g** = 200 near the ⟨001⟩ zone axis.

LPBF 316H TEM specimen was annealed at 600 °C inside the TEM for 90 minutes; the temperature and duration of the annealing are identical to the *in-situ* irradiation performed at 600 °C to 5 dpa. Figure 12 presents the elemental maps. Without irradiation, no Cr-rich oxides formed in the annealed sample, indicating that the formation of Cr-rich oxide in the irradiated LPBF 316H was an effect of irradiation. Oxygen enrichment at grain boundaries, however, were similar between the annealed and irradiated specimens. Conversely, a previous study on an LPBF 316L sample solution annealed at 1050 °C for 30 minutes also showed the formation of Cr-rich oxides [17]. Further investigation on the effects of irradiation and the thermal stability of the Cr-rich oxides is required.

The Cr and O maps in Figure 11 exhibit a denuded zone with a width of approximately 200 nm in the vicinity of the grain boundary. Along another grain boundary, however, the oxide-free denuded zone is less evident (Fig. 13). In addition, the density of oxide particles appears to be nonuniform among different grains. In Fig. 11, the number of Cr oxides appears to be greater in the upper-left grain than in the lower-right grain. Similar observations can also be made for the grains in Fig. 13.

Regarding the initial chemical inhomogeneity resulting from printing process, the depletion of Fe and the enrichment of Ni and Mo at cell walls largely continued after irradiation. The enrichment of Cr at the cell walls after irradiation, however, requires further investigation. Finally, the preexisting (Si, Mn) oxide nanoparticles inside the AM specimens remained after irradiation.

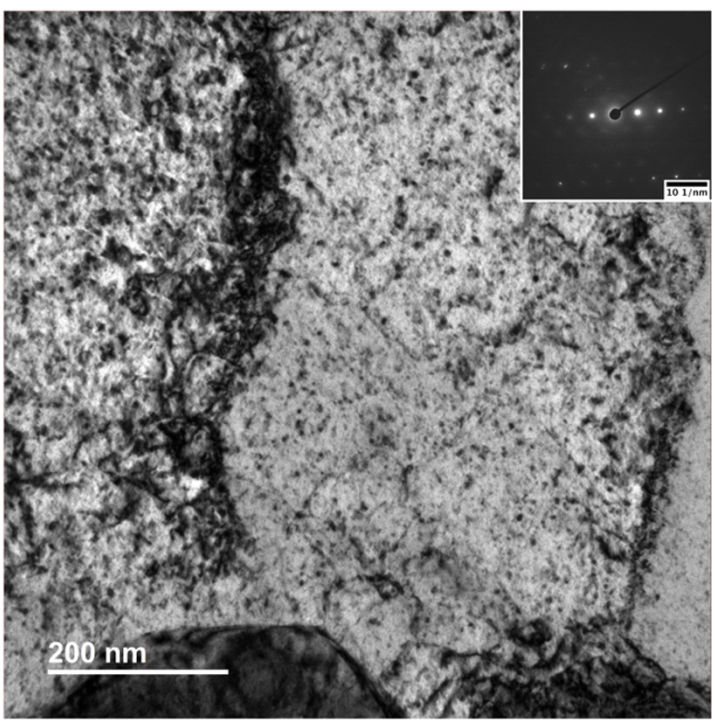

Figure 10: BF TEM image of LPBF 316L-2 in-situ irradiated with 1 MeV Kr ions at 300°C to 1 dpa. The inset diffraction pattern shows the imaging condition – a two-beam condition with $\mathbf{g} = 200$ near the $\langle 011 \rangle$ zone axis.

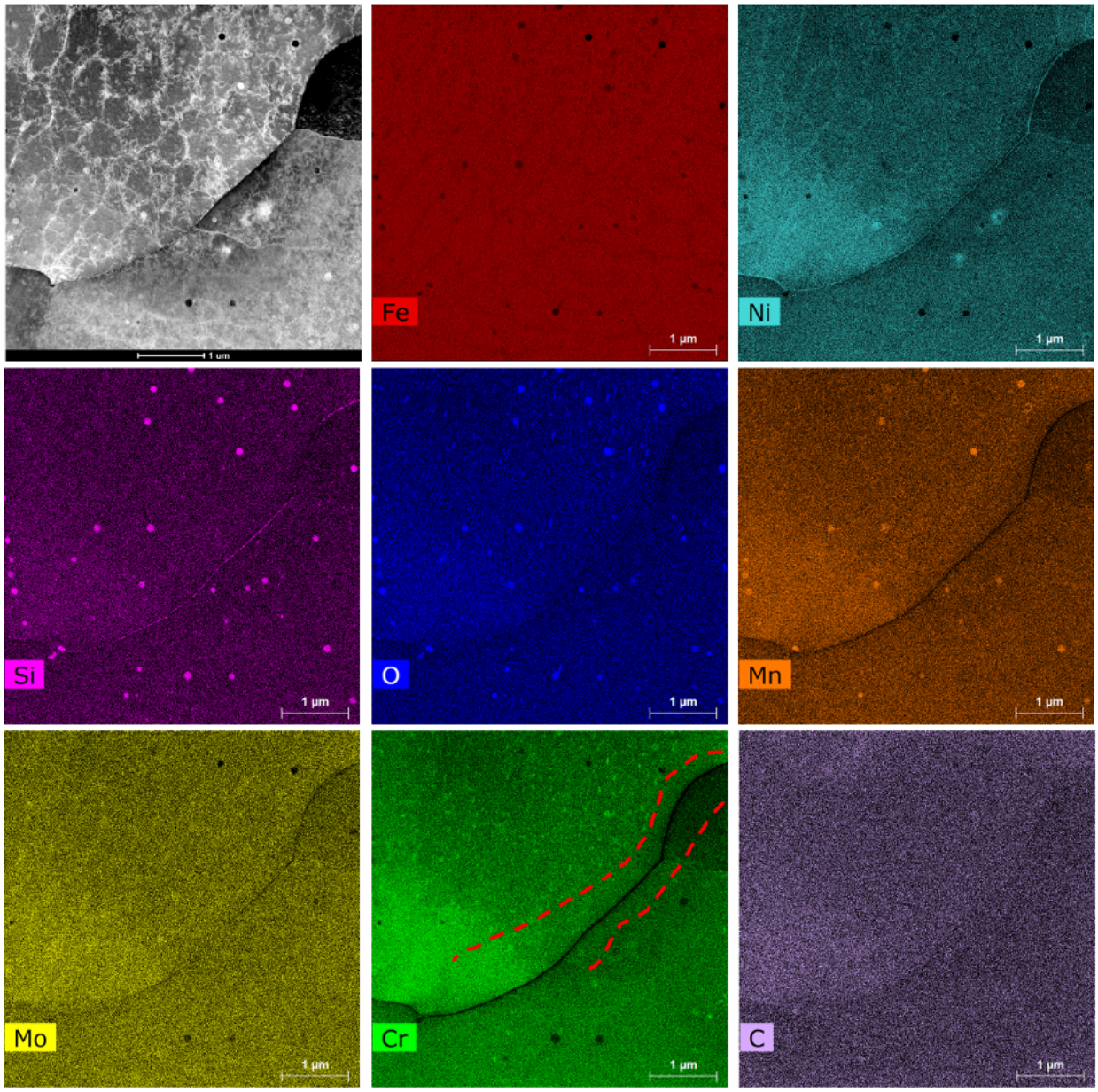

Figure 11: EDS maps of LPBF 316H in-situ irradiated at 600°C with 1 MeV Kr ions to 5 dpa. The red dashed curves highlight the boundary of a denuded zone of chromium oxides in the vicinity of the grain boundary. All the EDS maps are characteristic x-ray intensity maps, except for iron, which is a compositional map.

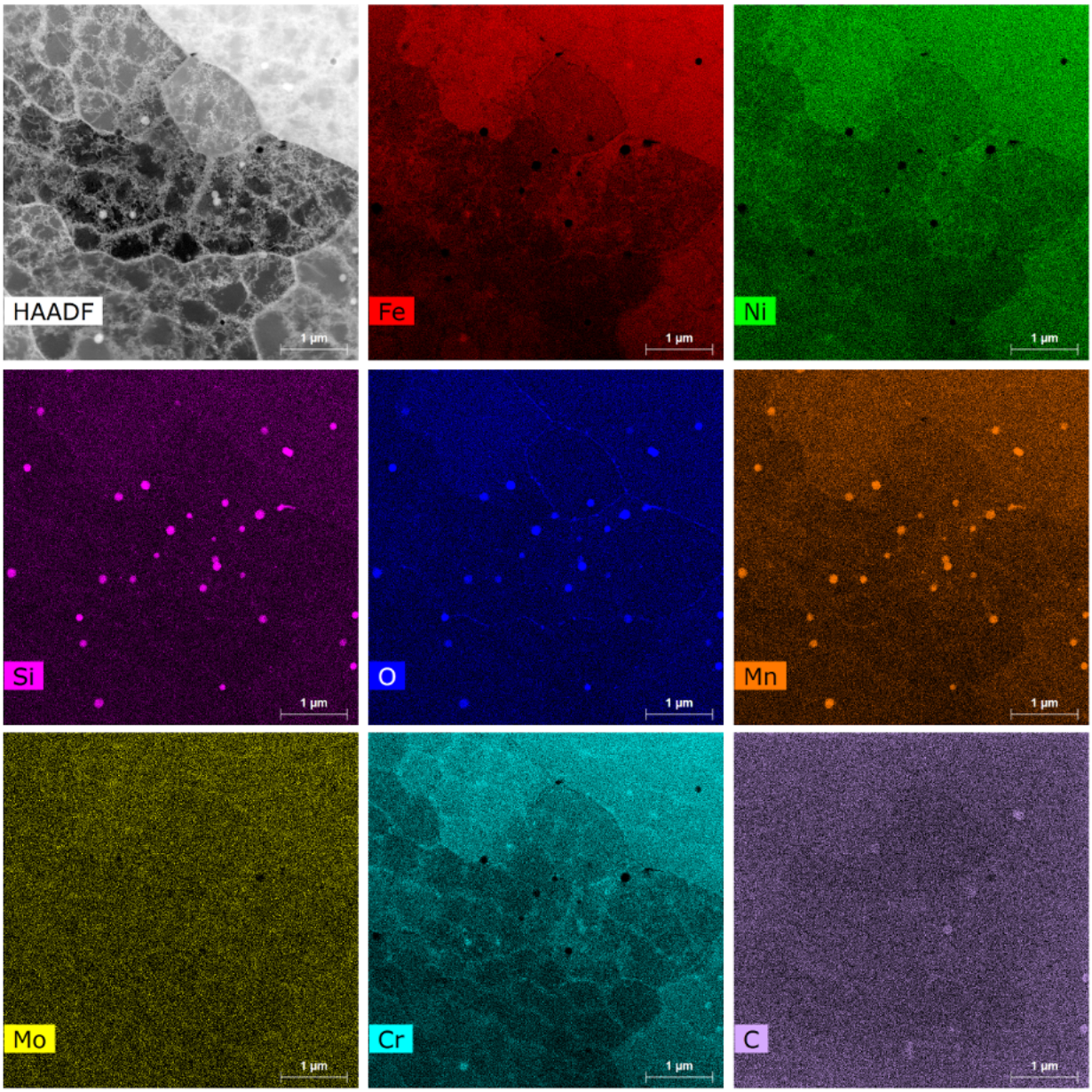

Figure 12: EDS maps of LPBF 316H annealed at 600°C inside a TEM for 90 minutes. All maps are intensity maps.

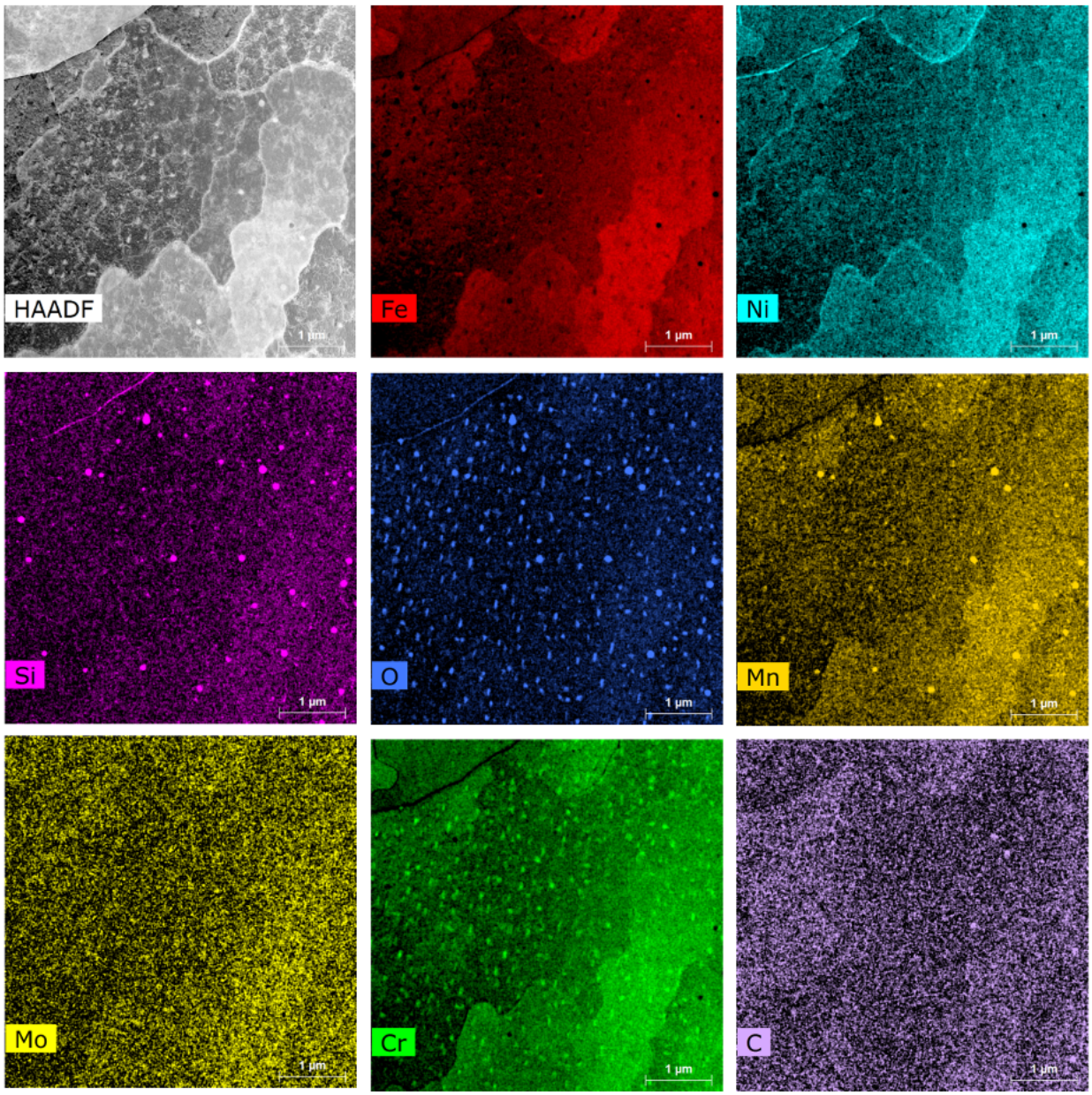

Figure 13: EDS maps of LPBF 316H in-situ irradiated at 600°C with 1 MeV Kr ions to 5 dpa. All elemental maps are characteristic x-ray intensity maps.

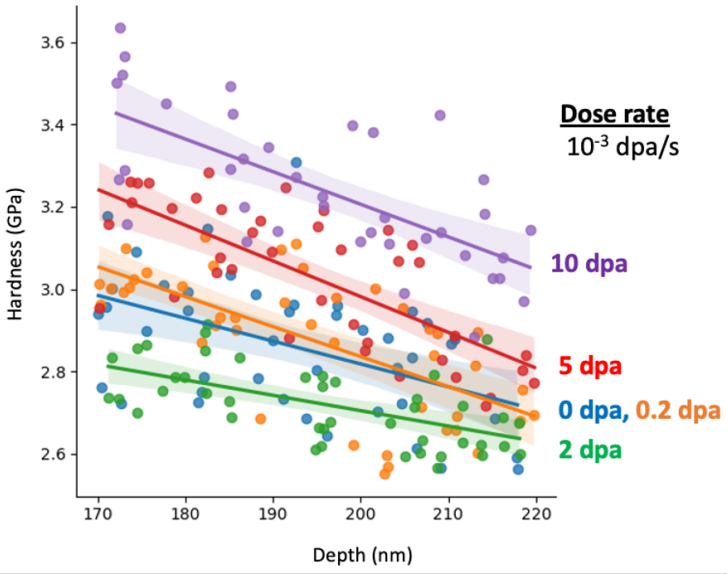

Figure 14: Load-controlled nanoindentation measurements on LPBF 316L-1 irradiated with 4 MeV Ni ions at 600°C.

2.5.4 Nanoindentation tests on *ex-situ* irradiated specimens

The *ex-situ* ion irradiations on LPBF 316L-1 shown in Table 3 have been completed. Nanoindentation tests were performed on the as-printed and 600 °C-irradiated specimens. The tests were carried out in a load-controlled mode with a maximum load of 4000 μN and a loading rate of 800 μN/s. Figure 14 shows the hardness as a function of contact depth. A general trend of decreasing hardness with increasing contact depth can be seen for all samples regardless their irradiation conditions. For all specimens, a considerable scattering of hardness data was observed. Therefore, sufficient data points must be collected to reveal any effect of irradiation dose. In the figure, the results from different doses are color coded. Each dot represents one indentation measurement. The lines are the linear regressions of the data at the given doses, and the shaded areas indicate the 95% confidence level around the regression line [18]. At 0.2 dpa, irradiation does not appear to affect the nanohardness. At 2 dpa, the hardness decreases slightly from the unirradiated state, indicating irradiation softening. At 5 and 10 dpa, the the hardness increased with irradiation dose over the unirradiated state. As compared with the as-printed specimen, the extent of hardening was about 11-14% for the range of contact depth explored. This complex dose dependence of nanohardness results is consistent with the recent tensile tests on neutron-irradiated AM samples [9].

3. Computational investigations

We integrate the ion irradiation results to guide our modeling investigation and provide feedback for experimental studies as part of our effort to understand the impact of microstructure and microchemical variability on radiation-driven microstructure evolution. We lay the foundation of accurate predictions of microstructure evolution with a novel mesoscale PF model using the MOOSE framework [5–7] to study defect migration and RIS in the unique dislocation cell structure present in AM 316 SS. To inform mesoscale simulations, we perform atomistic studies with molecular dynamics. We predict the partial diffusivity of vacancies and interstitial atoms in 316 stainless steel at a range of temperatures, which underpins the mesoscale phenomenon of radiation-induced segregation. We also examine the effect of carbon and chromium on collision cascade behavior to shed light on whether they impact radiation-driven microstructure evolution from the initial damage event.

3.1 Mesoscale phase field modeling of RIS in AM 316 SS

3.1.1 Model formulation for radiation-induced segregation

Following linear irreversible thermodynamics, the atomic and point defect transport can be described in terms of their chemical potential gradients $\boldsymbol{\nabla}\mu_i$. We define the concentrations as lattice site fractions, c, in the lattice frame of reference and choose Fe as the dependent species. We can thus reduce the number of components needed to be tracked to Ni, Cr, vacancy (V) and SIA (I) with $c_{Fe} = 1 - c_{Ni} - c_{Cr} - c_V + c_I$, and formulate the fluxes in terms of the diffusion potential $\tilde{\mu}_i = \mu_i - \mu_{Fe}$ gradients as

$$\boldsymbol{J}_{Ni} = -\left(\tilde{L}_{NiNi}\boldsymbol{\nabla}\tilde{\mu}_{Ni} + \tilde{L}_{NiCr}\boldsymbol{\nabla}\tilde{\mu}_{Cr} + L_{NiV}\boldsymbol{\nabla}\mu_V\right), \tag{1a}$$

$$\boldsymbol{J}_{Cr} = -\left(\tilde{L}_{CrNi}\boldsymbol{\nabla}\tilde{\mu}_{Ni} + \tilde{L}_{CrCr}\boldsymbol{\nabla}\tilde{\mu}_{Cr} + L_{CrV}\boldsymbol{\nabla}\mu_V\right), \tag{1b}$$

$$\boldsymbol{J}_{V} = -\left(\tilde{L}_{VNi}\boldsymbol{\nabla}\tilde{\mu}_{Ni} + \tilde{L}_{VCr}\boldsymbol{\nabla}\tilde{\mu}_{Cr} + L_{VV}\boldsymbol{\nabla}\mu_V\right), \tag{1c}$$

$$\boldsymbol{J}_{I} = -\left(\tilde{L}_{INi}\boldsymbol{\nabla}\tilde{\mu}_{Ni} + \tilde{L}_{ICr}\boldsymbol{\nabla}\tilde{\mu}_{Cr} + L_{II}\boldsymbol{\nabla}\mu_I\right), \tag{1d}$$

where $\boldsymbol{J}_{Fe} + \boldsymbol{J}_{Cr} + \boldsymbol{J}_{Ni} + \boldsymbol{J}_V - \boldsymbol{J}_I = 0$. The above form of force-flux relations are consistent with Cahn-Hilliard type equations proposed for RIS in a binary body centered cubic (BCC) Fe–Cr alloy [19].

$\tilde{L}$ or $L^{(Fe)}$ are the relative transport coefficients given by $\tilde{L}_{kl} = L^V_{kl} + L^I_{kl} - c_l(L_{kV} + L_{kI})$, $\tilde{L}_{Vl} = -\sum_k L^V_{kl} + c_l L_{VV}$ and $\tilde{L}_{Il} = \sum_k L^I_{kl} - c_l L_{VV}$. From Onsager's reciprocity, $L_{kl} = L_{lk}$, $L_{Vl} = L_{lV} = -\sum_k L^V_{kl}$, $L_{Il} = \sum_k L^I_{kl}$ and $\tilde{L}_{\nu\nu} = \sum_k \sum_l L^\nu_{kl}$. The Onsager coefficients L^d_{kl} are expressed using Manning's relation as [20]

$$L^\nu_{kl} = c_k c_\nu d_{k\nu}\left(\delta_{kl} + \frac{2c_l d_{l\nu}}{M_o \sum_i c_i d_{i\nu}}\right), \tag{2}$$

where $d_{k\nu}$ is the partial diffusion coefficient, δ_{kl} is the Kronecker delta and $M_\circ = 2f_\circ/(1 - f_\circ)$,

with $f_\circ$ being geometric correlation factor for fcc structures. In the present work, we describe the vacancy partial diffusion coefficient from experimentally-fit tracer diffusion or atomic mobility data as

$$d_{kV} = M_k^\circ \exp\left(\frac{-Q_k + E_V^f}{k_B T}\right), \tag{3}$$

where $M_k^\circ = \exp(\Theta_k)$ is the frequency factor, Q_k is the activation energy and E_V^f is the vacancy formation energy. The Redlich-Kister coefficients in the expressions for Θ_k and Q_k are obtained from Ref. [21]. The self-interstitial partial diffusion coefficients are given by the Arrhenius-type dependence as

$$d_{kI} = \frac{1}{6}\lambda_I^2 z f_I \omega_{kI}^\circ \exp\left(-\frac{E_I^m}{k_B T}\right)\tilde{\beta}_{kI} \tag{4}$$

where λ_I is the jump distance of I, z_I is the site coordination number, ω_{kI}° is the prefactor for jump frequency, E_I^m is the interstitial migration energy (assumed to be same for all atomic elements) and $\tilde{\beta}_{kI} = \exp((E_{kI} - E_{FeI})/k_B T))/\left\{c_{Fe} + \sum_k c_k \exp((E_{kI} - E_{FeI})/k_B T)\right\}$ is the interstitial binding factor for k as per Ref. [22].

The concentration evolutions are given by the mean-field reaction-rate-theory as

$$\frac{\partial c_{Ni}}{\partial t} = -\boldsymbol{\nabla}.\boldsymbol{J}_{Ni}, \tag{5a}$$

$$\frac{\partial c_{Cr}}{\partial t} = -\boldsymbol{\nabla}.\boldsymbol{J}_{Cr}, \tag{5b}$$

$$\frac{\partial c_V}{\partial t} = -\boldsymbol{\nabla}.\boldsymbol{J}_V + \dot{P}_V - \dot{S}_V(c_V - c_v^e) - \dot{R}_{VI} c_V c_I, \tag{5c}$$

$$\frac{\partial c_I}{\partial t} = -\boldsymbol{\nabla}.\boldsymbol{J}_I + \dot{P}_I - \dot{S}_I(c_I - c_I^e) - \dot{R}_{VI} c_V c_I, \tag{5d}$$

where $\dot{P}_V = \dot{P}_I = \epsilon \dot{P}_\circ$ is the defect production rate, ϵ is the displacement efficiency and $\dot{P}_\circ$ is the irradiation damage rate in dpa [23]. $\dot{R}_{VI} = 4\pi r_\circ (D_{VV} + D_{II})/v_\circ$ is the vacancy-interstitial recombination rate with $r_\circ$ being the recombination radius. The point defect absorption rate $\dot{S}_v$ of a symmetric tilt GB consisting of an array of parallel dislocations with spacing d_{disl} is given by [24, 25]

$$\dot{S}_v^{gb} = \frac{2\pi D_{vv}}{d_{\text{disl}}^2 \log(d_{\text{disl}}/2b)}, \tag{6}$$

where $d_{\text{disl}} = b/(2\sin(\Delta\alpha/2))$. $\Delta\alpha$ is difference in misorientation angle from zero degree or the angle of a Σ-boundary and $b = a_\circ/\sqrt{\Sigma}$. The sink absorption rate of dislocations are given by

$$\dot{S}_v^{disl} = \frac{4\pi r_v^c}{d_\circ}\rho_{\text{disl}} D_{vv}, \tag{7}$$

where ρ_{disl} is the dislocation number density. r_ν^c the sink capture radius, and $d_\circ$ the interplanar spacing [26, 27]. The vacancy and interstitial diffusivities are given by $D_{\nu\nu} = c_{Ni} d_{Ni\nu} + c_{Cr} d_{Cr\nu} + c_{Fe} d_{Fe\nu}$.

A multi-order phase field model is employed to describe the AM microstructure consisting of multiple dislocation cells. A system of p dislocation cells is represented by the set of order parameters fields $\eta_1, \eta_2, \ldots, \eta_p$, with the characteristic order parameter for cell i denoted by η_{mi}. The region in cell i is defined by $\eta_i = 1$ and $\eta_j = 0$ ($\forall j \neq i$). The total free energy of the system is written as

$$\mathcal{F} = \int_V \left[f_{\text{alloy+defect}}(\boldsymbol{c}) + f_{\text{disl}}(\boldsymbol{\eta}) + w g(\boldsymbol{\eta}) + \frac{\kappa}{2} |\nabla \boldsymbol{\eta}|^2 \right] \mathrm{d}V, \tag{8}$$

Here, $f_{\text{alloy+defect}}(\boldsymbol{c}) \approx f_{\text{alloy}}(c_{Ni}, c_{Cr}) + f_{\text{defect}}(c_V, c_I)$ is the free energy of the Fe–Ni–Cr solid solution with irradiation-induced vacancies (V) and self-interstitials (I), given by

$$\begin{aligned} f_{\text{alloy}} \approx & f^\circ_{\text{FeNiCr}} + \tilde{\mu}^\circ_{Ni}(c_{Ni} - c^\circ_{Ni}) + \tilde{\mu}^\circ_{Cr}(c_{Cr} - c^\circ_{Cr}) \\ & + \frac{\tilde{\theta}^\circ_{NiNi}}{2}(c_{Ni} - c^\circ_{Ni})^2 + \frac{\tilde{\theta}^\circ_{CrCr}}{2}(c_{Cr} - c^\circ_{Cr})^2 + \tilde{\theta}^\circ_{NiCr}(c_{Ni} - c^\circ_{Ni})(c_{Cr} - c^\circ_{Cr}), \end{aligned} \tag{9a}$$

$$f_{\text{defect}} \approx E_V^f c_V + E_I^f c_I + \frac{RT}{v_m}\left(c_V \ln c_V + c_I \ln c_I\right). \tag{9b}$$

f_{alloy} has been approximated using the second-order Taylor expansion of the CALPHAD-based Fe–Ni–Cr free energy (f_{TC}) about the nominal alloy composition $\mathbf{c}^\circ = \{c^\circ_{Ni}, c^\circ_{Cr}\}$. The fitting parameters are $f^\circ_{\text{FeNiCr}} = f_{\text{TC}}(\mathbf{c}^\circ)$, $\tilde{\mu}^\circ_k = \partial f_{\text{TC}}/\partial c_k\big|_{\mathbf{c}^\circ}$ and $\tilde{\theta}^\circ_{kl} = \partial^2 f_{\text{TC}}/\partial c_k \partial c_l\big|_{\mathbf{c}^\circ}$. f_{defect} has been approximated in the dilute limit. The thermal equilibrium concentration of a point defect is given by $c_\nu^e \approx \exp\left(-E_\nu^f/k_B T\right)$, and E_ν^f is the formation energy of defect ν in face centered cubic (FCC) Fe–Ni–Cr.

The free energy contribution from the dislocation distribution in the microstructure f_{disl} is expressed as

$$f_{\text{disl}} = \frac{1}{2} G b^2 \left[(1 - g_\circ)\rho_{\text{bulk}} + g_\circ \rho_{\text{wall}}\right], \tag{10}$$

where ρ_{bulk} is the loop dislocation density within the bulk of cells and ρ_{wall} is the network dislocation density at the cell wall. To distinguish the dislocation densities within individual cells, ρ_i, the former is expressed as $\rho_{\text{bulk}} = \sum \rho_i h_i / \sum h_i$, where $h_i(\boldsymbol{\eta}) = \eta_i^2$ [6]. $g_\circ = 8g(\boldsymbol{\eta})$ is employed as a normalized interpolation function to represent the network dislocation or cell wall structure. $g(\boldsymbol{\eta})$, as defined here and in Eq. 8, is a multi-well potential defined for symmetric interfaces (i.e. $\eta_i = 1 - \eta_j$) in the multi-order-parameter model [28] as

$$g = \frac{1}{4} + \sum_{i=1}^{p}\left(\frac{\eta_i^4}{4} - \frac{\eta_i^2}{2}\right) + 1.5\sum_{i=1}^{p}\sum_{j=1, j\neq i}^{p} \eta_i^2 \eta_j^2. \tag{11}$$

The diffusion potentials in the flux relations (Eqs. 1) can derived from the free energy functional (Eq. 8) using variational principles as $\tilde{\mu}_k = \delta F/\delta c_k$ and $\tilde{\mu}_\nu = \delta F/\delta c_\nu$. Using the transport fluxes and the free energy function, the evolution equations for concentrations in the diffusion form and the order parameters in Allen-Cahn form can be derived as

$$\frac{\partial c_{Ni}}{\partial t} = \boldsymbol{\nabla}.\left(\tilde{D}_{NiNi}\boldsymbol{\nabla}c_{Ni} + \tilde{D}_{NiCr}\boldsymbol{\nabla}c_{Cr} + D_{NiV}\boldsymbol{\nabla}c_V + D_{NiI}\boldsymbol{\nabla}c_I\right), \tag{12a}$$

$$\frac{\partial c_{Cr}}{\partial t} = -\boldsymbol{\nabla}.\left(\tilde{D}_{CrNi}\boldsymbol{\nabla}c_{Ni} + \tilde{D}_{CrCr}\boldsymbol{\nabla}c_{Cr} + D_{CrV}\boldsymbol{\nabla}c_V + D_{CrI}\boldsymbol{\nabla}c_I\right), \tag{12b}$$

$$\frac{\partial\, c_V}{\partial t} = -\boldsymbol{\nabla}.\left(\tilde{D}_{VNi}\boldsymbol{\nabla}c_{Ni} + \tilde{D}_{VCr}\boldsymbol{\nabla}c_{Cr} + D_{VV}\boldsymbol{\nabla}c_V\right) + \dot{P}_V - \dot{S}_V(c_V - c_V^e)g(\boldsymbol{\eta}) - \dot{R}_{VI}c_V c_I, \tag{12c}$$

$$\frac{\partial\, c_I}{\partial t} = -\boldsymbol{\nabla}.\left(\tilde{D}_{INi}\boldsymbol{\nabla}c_{Ni} + \tilde{D}_{ICr}\boldsymbol{\nabla}c_{Cr} + D_{II}\boldsymbol{\nabla}c_I\right) + \dot{P}_I - \dot{S}_I(c_I - c_I^e)g(\boldsymbol{\eta}) - \dot{R}_{VI}c_V c_I, \tag{12d}$$

$$\frac{\partial\, \eta}{\partial t} = -L_\eta\left(\frac{df_{disl}}{d\eta_i} + w\frac{dg}{d\eta_i} - \kappa\nabla^2\eta_i\right). \tag{12e}$$

The diffusivities are given in terms of the Onsager coefficients and thermodynamic factors as $\tilde{D}_{kl} = \sum_{m=Ni,Cr}\tilde{L}_{km}\tilde{\theta}_{ml}$, for $k,l = \{\text{Ni, Cr, V, I}\}$ and $D_{k\nu} = L_{k\nu}\theta_{\nu\nu}$, for $\nu = \{\text{V, I}\}$. By definition, the atomic thermodynamic factors $\tilde{\theta}_{ml}$ are equivalent to the nominal values $\tilde{\theta}^\circ_{ml}$ of the Taylor free energy, Eq. 9a. However, to prevent concentrations from taking unphysical values, such as during RIS at high-angle GB in large-grained systems, we introduce concentration dependence based on an ideal thermodynamic model as $\tilde{\theta}_{NiCr} = \tilde{\theta}_{CrNi} = \tilde{\theta}^*_{NiCr}/c_{Fe}$, $\tilde{\theta}_{NiNi} = \tilde{\theta}^*_{NiNi}(1 - c_{Cr})/c_{Fe}$ and $\tilde{\theta}_{CrCr} = \tilde{\theta}^*_{CrCr}(1 - c_{Ni})/c_{Fe}$. Here, $\tilde{\theta}^*$ are the normalized factors calculated at nominal alloy composition as $\tilde{\theta}^*_{NiCr} = \tilde{\theta}^*_{CrNi} = \tilde{\theta}^\circ_{NiCr}c^\circ_{Fe}$, $\tilde{\theta}^*_{NiNi} = \tilde{\theta}^\circ_{NiNi}c^\circ_{Fe}/(1 - c^\circ_{Cr})$ and $\tilde{\theta}^*_{CrCr} = \tilde{\theta}^\circ_{CrCr}c^\circ_{Fe}/(1 - c^\circ_{Ni})$. The thermodynamic factor for a point defect species is given by $\tilde{\theta}_{\nu\nu} = (RT/v_m)/c_\nu$. The derivatives in Eq. (12e), governing the driving force for microstructure evolution, are given by

$$\frac{df_{\text{disl}}}{d\eta_i} = \frac{Gb^2}{2}\left[(1 - g_\circ)\frac{\partial h_i}{\partial\eta_i}\frac{(\rho_i - \rho_{bulk})}{\sum_j h_j} + (\rho_{\text{wall}} - \rho_{\text{bulk}})\frac{\partial g_\circ}{\partial\eta_i}\right], \tag{13a}$$

$$\frac{dg}{d\eta_i} = \eta_i^3 - \eta_i + 3\eta_i\sum_j\eta_j^2, \tag{13b}$$

$$\frac{dh}{d\eta_i} = 2\eta_i. \tag{13c}$$

3.1.2 Radiation-induced segregation model parameterization

For an planar interface in equilibrium, the dislocation wall energy σ_{wall} and width $2\Delta_{\text{wall}}$ can be derived following the general method in Ref. [29] as

$$\sigma_{\text{wall}} = \frac{4}{3}\sqrt{\left(\frac{1}{2}Gb^2\rho_{\text{wall}} + w_{\text{wall}}\right)\kappa_{\text{wall}}}, \tag{14a}$$

$$2\Delta_{\text{wall}} = \sqrt{\frac{8\kappa_{\text{wall}}}{(4Gb^2\rho_{\text{wall}} + w_{\text{wall}})}}. \tag{14b}$$

Considering all the energetic contribution of the cell wall is due to the dislocation energy density, we set $w = 0$. This allows the model parameter κ to be determined from Eq. 14b and gives $\sigma_{\text{wall}} = (2/3)Gb^2\rho_{\text{wall}}\Delta_{\text{wall}}$ from Eq. 14a. Within the phase field formulation, ρ_{wall} is the (maximum) dislocation density at the center of the cell wall. The GB energy σ_{gb} and width $2\Delta_{\text{gb}}$ are expressed in terms of model parameters as [29]

$$\sigma_{\text{gb}} = \frac{4}{3}\sqrt{w_{\text{gb}}\kappa_{\text{gb}}}, \tag{15a}$$

$$2\Delta_{\text{gb}} = \sqrt{\frac{8\kappa_{\text{gb}}}{w_{\text{gb}}}}. \tag{15b}$$

Here, we use a physically-based value for σ_{gb} and set $2\Delta_{\text{gb}}$ to a numerically feasible value to determine w_{gb} and κ_{gb} in Table 4.

The RIS model was parameterized for FCC Fe–12Ni–17Cr by adapting and re-tuning the parameters of Yang et al. [21] to the current composition and non-ideal PF model. The optimized functions for the composition-dependence of the activation energy Q_i and the pre-factor exponent Θ_i under thermal conditions are obtained from Ref. [21]. The vacancy migration energy is given by the difference $E^m_{Vi} = Q_i - E^f_V$, where E^f_V is an uncertain parameter that needs to be parameterized based on atomistic calculations. Q_i falls in the range 2.84–2.97 eV; $E^f_V = 1.8$ eV is chosen based on the first principles study of Ref. [30]; and $S^f_V = 2k_B$ is assumed. This yields an effective migration free energy in the range 1.2–1.25 at 873 K. The vacancy diffusion coefficients at 873 K are obtained as $D_{VV} \approx 2.2 \times 10^6$ nm^2/s, $d_{CrV}/d_{NiV} = 2.63$ and $d_{FeV}/d_{NiV} = 1.64$. The ratios of vacancy partial diffusion coefficients agree well with the general range reported in Ref. [21], and describe the faster Cr and slower Ni transport in FCC Fe via the vacancy-atom exchange mechanism.

The migration energies for all atomic species via the interstitial mechanism is assumed to be equal with E^m_I = 0.6 eV. A higher value of E^m_I = 0.9 eV was used for Fe-rich alloys in Ref. [21], which resulted in a lower diffusivity for SIAs compared to vacancies. Setting E^m_I = 0.6 eV in the present work yields $D_{II} \approx 2.8 \times 10^7$ nm^2/s at 873 K, which is an order of magnitude faster than D_{VV}. First principles studies of SIA formation in dilute [30] and concentrated [31] FCC Fe–Ni–Cr indicate attractive interaction with Cr, repulsive interaction with Ni and a near-ideal

interaction with Fe. The positive value of $E^b_{CrI} - E^b_{FeI} = 0.025$ eV models favorable transport via Cr interstitials whereas the negative value of $E^b_{NiI} - E^b_{FeI} \approx -0.008$ models unfavorable transport via Ni interstitials. These values were slightly modified from those in Ref. [21] to better capture the RIS-temperature trends for the current composition of interest. The resulting binding factors for the SIA partial diffusivities are $\beta_{CrI} = 1.31$, $\beta_{NiI} = 0.85$ and $\beta_{FeI} = 0.94$. The ratios of SIA partial diffusion coefficients are obtained as $d_{CrI}/d_{NiI} = 1.54$ and $d_{FeI}/d_{NiI} = 1.1$, which describe favorable transport of Cr interstitials and an unfavorable transport of Ni interstitials. While there are uncertainties in the SIA parameters, the vacancy-mediated transport is expected to dominate the RIS behavior, except at lower temperatures.

Table 4: Default parameter values used in phase field radiation-induced segregation model.

Property	Value	Ref.	Property	Value	Ref.
c°_{Ni}	0.12		$a_\circ$	0.35 nm	[32]
c°_{Cr}	0.17		v_m	$N_A a^3_\circ/4$ cm^3/mol	[1]
T	773 K		λ_I	0.25 nm	[1]
E^f_V	1.8 eV	[21]	z	12	[33]
S^f_V	$2\,k_B$	[1]	f_I	0.44	[33]
E^f_I	3.6 eV	[33]	ω°_{kI}	1.5×10^{12} s^{-1}	[33]
E^m_I	0.6 eV	[21]	$\dot{P}_\circ$	7×10^{-6} s^{-1}	[23]
$E^b_{CrI} - E^b_{FeI}$	0.025 eV	[21]	$f_\circ$	0.78	[34]
$E^b_{NiI} - E^b_{FeI}$	-0.0075 eV	[21]	$v_\circ$	$a^3_\circ/4$ Å^3	[1]
$\tilde{\theta}^\circ_{NiNi}$	$0.95 \times (RT/v_m)$	[35]	G	73 GPa	[36]
$\tilde{\theta}^\circ_{CrCr}$	$1.04 \times (RT/v_m)$	[35]	b	0.5 nm	
$\tilde{\theta}^\circ_{NiCr}$	$1.42 \times (RT/v_m)$	[35]	$2\Delta_{\text{gb}}$	5 nm	
$d_\circ$	$a_\circ$		σ_{gb}	1 J/m^2	
$r_\circ$	$2a_\circ$		$2\Delta_{\text{wall}}$	100, 200 nm	[11]
r^c_v	$2d_\circ$		κ_{wall}	1.3, 5.4 $\times 10^{-8}$ J/m	
ρ_{bulk}	10^{-4} nm^{-2}	[33]	κ_{gb}	3.8×10^{-9} J/m^3	
ρ_{wall}	10^{-3} nm^{-2}	[37]	w_{gb}	1.2×10^{9} J/m^3	
L_η	1×10^{-11} m^3/(Js)				

3.1.3 Results of scaling dislocation cell wall widths on simulated RIS

The diffuse order parameters representing the GB and dislocation cell wall in the PF simulation are shown for a one-dimensional (1D) system in Fig. 15. Widths on the order of a few nm and 100 nm were employed for the GB and cell wall, respectively, with the dislocation cell wall width informed by the experimental investigations in Section 2. RIS results using four different PF widths are compared and verified against the conventional sharp interface RIS model in Fig. 16. While the PF model describes the sink via a local defect absorption rate term, $\dot{S}_v(c_V - c^e_V)g(\boldsymbol{\eta})$,

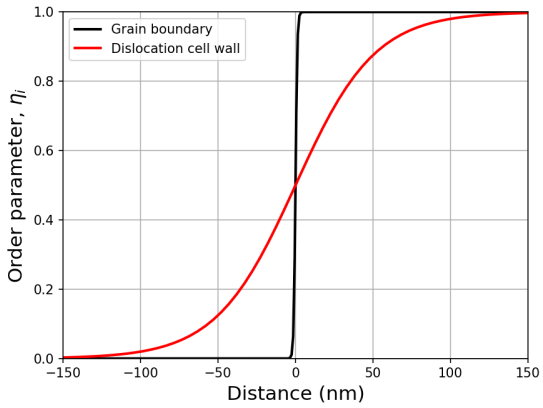

Figure 15: Diffuse interface representation of a GB and a dislocation cell wall with order parameters of widths 5 nm and 100 nm, respectively.

the sharp interface model assumes an ideal sink and imposes the equilibrium point defect concentration at the GB location via a Dirichlet boundary condition, $c_\nu = c_\nu^e$. RIS profiles for 5 nm wide interface matched well with the results from the sharp-interface simulation. While smaller widths require a finer mesh, making the simulation more expensive, larger widths with the same sink absorption rate resulted in wider RIS profiles.

The dislocation density distribution across the PF cell wall is shown in Fig. 17. The total dislocation density ρ_{tot} is the integrated value across the PF cell wall. Based on experimental characterization, the physical width of the cell wall is 100 nm. If the PF width is set to $2\Delta_{\text{wall}} = 100$ nm and the peak dislocation density ρ_{wall} is set to a physical value of $\rho_{\text{phys}} = 10^{-3}$ nm^{-2}, we obtain $\rho_{\text{tot}} = 0.05$ nm^{-1}, which is half the physical total dislocation density 100 $\rho_{\text{phys}} = 0.1$ nm^{-1}. To realize $\rho_{\text{tot}} = 100\ \rho_{\text{phys}}$, we can either fix $2\Delta_{\text{wall}} = 100$ nm and determine ρ_{wall} or set $\rho_{\text{wall}} = \rho_{\text{phys}}$ and determine $2\Delta_{\text{wall}}$. Steady-state RIS profiles for all these cases are shown in Fig. 17b. The first case with $\rho_{\text{tot}} < 0.1$ nm^{-1} clearly shows lower RIS. Among the other two cases, the former with $\rho_{\text{wall}} > \rho_{\text{phys}}$ shows greater RIS. We choose the case where $\rho_{\text{wall}} = \rho_{\text{phys}}$ and $2\Delta_{\text{wall}} \approx 200$ nm. RIS at the dislocation cell wall in Fig. 17b is found to be be lower in peak value and wider in profile compared to that of a general high angle grain boundary (HAGB). A more detailed study is warranted to determine effective parameters for ρ_{wall} and $2\Delta_{\text{wall}}$ that yield physically representative RIS peak concentration or excess.

3.1.4 Results of sink strength dependence of RIS at grain boundaries

To effectively model RIS at GBs, it is necessary to describe the GB sink behavior physically. The sink strength $\dot{S}_\nu^{\text{gb}} / D_\nu$ of a geometrically simple symmetric tilt GB is modeled as a function of line dislocation spacing using Eq. 6, where the dislocations are assumed to be perfect sinks. RIS profiles and peak GB concentrations for a range of misorientation angles $\alpha = 0 - 21^\circ$ are plotted in Figs. 18a and b, respectively. With an increase in α, the dislocation spacing decreases,

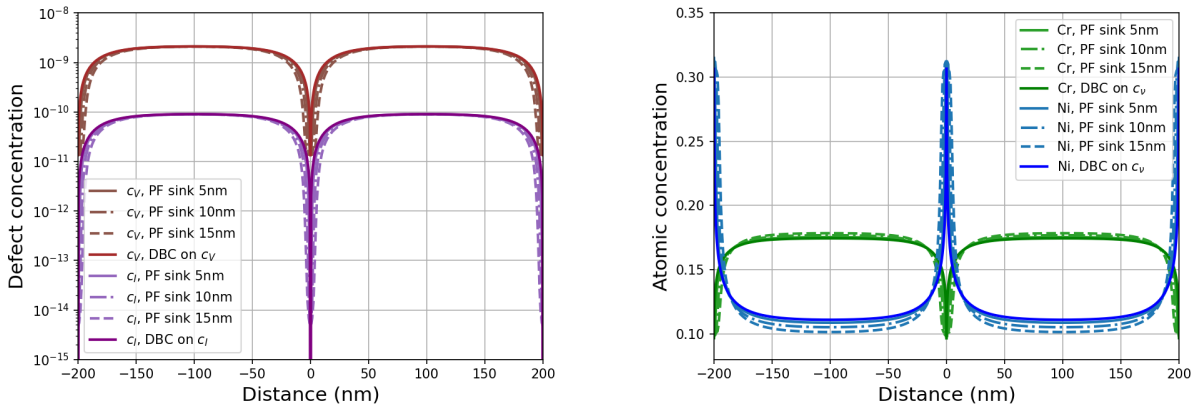

(a) (b)

Figure 16: Steady-state concentration profiles for (a) point defects and (b) atomic components in a periodic 1D system with a general HAGB at -200, 0 and 200 nm. "DBC" refers to the Dirichlet boundary condition used for a sharp-interface solution. Default RIS model parameters in Table 4 were used.

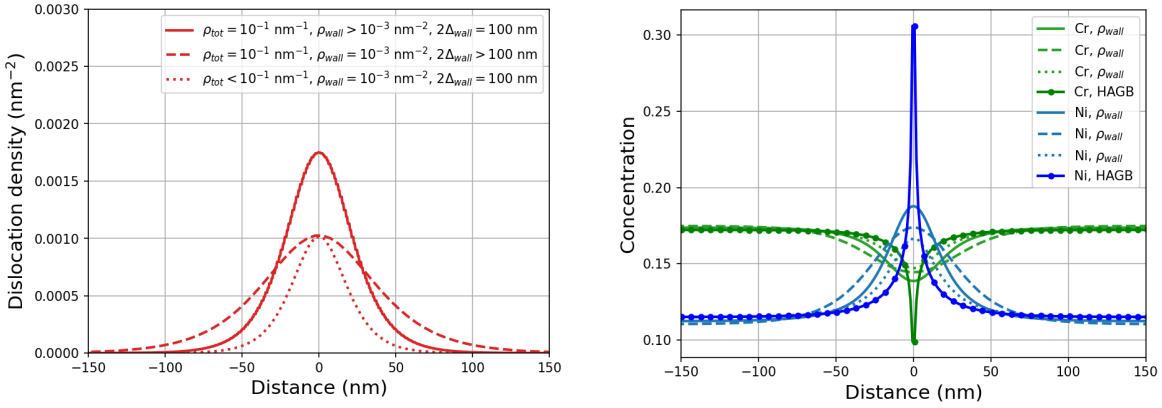

(a) (b)

Figure 17: (a) Dislocation network density variation across the cell wall in the PF model realized for different parameters: total dislocation density ρ_{tot} across cell wall, maximum dislocation density ρ_{wall} and cell wall width $2\Delta_{\text{wall}}$. (b) RIS at cell wall for parameters in (a) compared against RIS at a general HAGB.

leading to greater sink strengths, and therefore, greater RIS. Symmetric HAGBs are expected to behave similar to ideal sinks with $\dot{S}_v^{gb}/D_v > 25$ nm^{-2} for $\alpha > 21°$. Indeed for these GBs, the point defect concentrations at the GB center are maintained at their equilibrium value c_v^e (akin to conventional RIS models with a Dirichlet boundary condition), and the RIS peak concentrations or their excess attain a constant maximum value. For lower α, the GBs behave as imperfect sinks and exhibit little RIS; for instance, $\theta = 3.7°$ exhibits a low sink strength of $\dot{S}_v^{gb}/D_v \approx 0.1$ nm^{-2}, in agreement with Ref. [38]. We note here that the sink strength $\dot{S}_v/D_v$ has been defined in the PF model as a local value at the spatially resolved sink. In contrast, some diffusion or rate theory models tend to define mean-field sink strengths assuming a geometric distribution for the GBs. In Fig. 17b, the mean-field sink strength $\dot{S}_v^{disl}/D_v$ of dislocations with a density of $\rho_{wall} = 10^{-4}$ nm^{-2} is 0.0025 nm^{-2} and that for 10^{-3} nm^{-2} is 0.025 nm^{-2}.

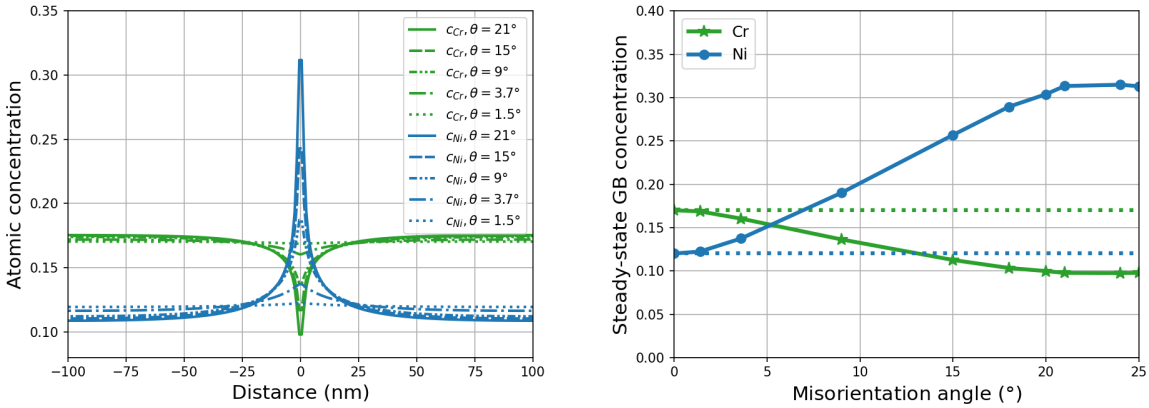

(a) (b)

Figure 18: (a) Steady-state atomic concentration profiles for different symmetric tilt GBs in a 1D system. (b) Peak RIS concentrations as a function of the GB misorientation angle. Default RIS model parameters in Table 4 were used.

3.1.5 Results of effect of temperature and dose rate on RIS

The time evolution of RIS at the GB is shown in Fig. 20a for different dose rates. With an increase in dose rate, the time to reach steady state decreases. Indeed, irradiations using ions take considerably less time (several hours) to reach the same damage rate or extent of RIS compared to neutrons (several years). Steady-state RIS at the GB is shown as a function of temperature for different dose rates in Fig. 20b. For a given dose rate, RIS reaches a maximum at some intermediate temperature. The low RIS at low temperatures can be attributed to the dominant effect of defect recombination and at high temperatures to the thermal back diffusion. The temperature to reach maximum RIS is seen to shift to higher temperatures for higher dose rates; this is consistent with theory [1] and modeling results [39], and can been attributed to the trade-off between athermal dose rate and thermal kinetic effects. While the dose (dpa) to reach steady state is similar if

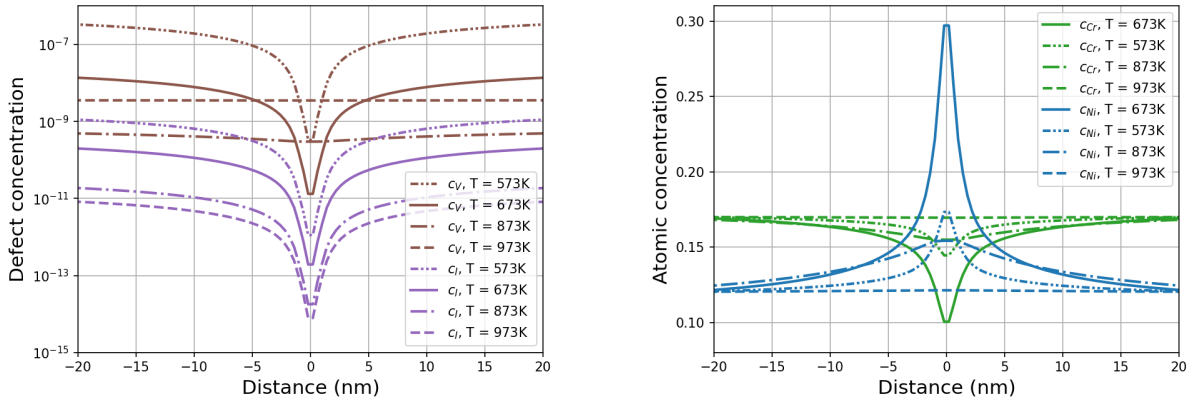

(a) (b)

Figure 19: Effect of temperature on the steady-state concentration profiles of (a) point defects and (b) atomic components in a periodic 1D system (see Fig. 16 with a general HAGB. Default RIS model parameters of Table 4 were used.

the same displacement efficiency is assumed, each irradiation particle type is expected to have a different displacement efficiency, and the nominal dose rate will need to be corrected in future work to an efficiency-corrected value.

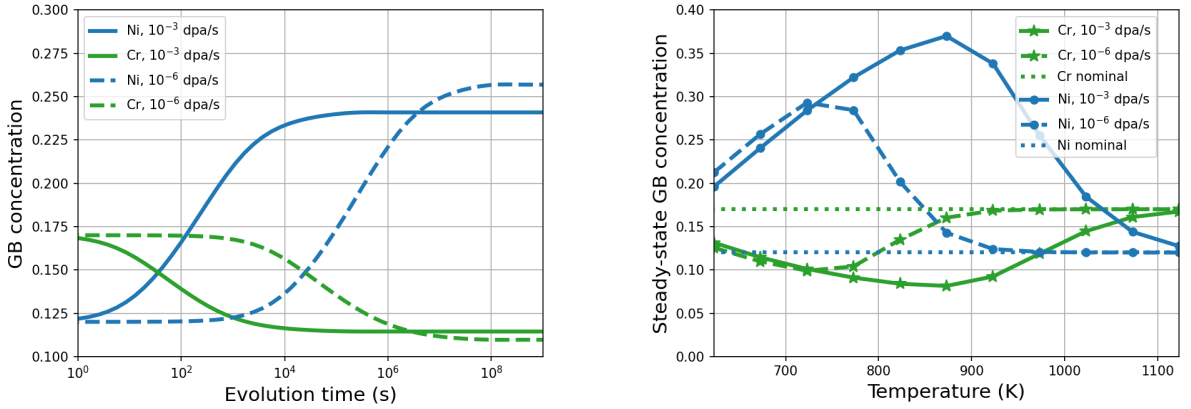

(a) (b)

Figure 20: Effect of irradiation dose rate or particle type on RIS. (a) Time to reach steady state concentration at 673 K. (b) Combined effect of temperature and dose rate on the steady-state GB concentration. Default values from Table 4 were used for other model parameters.

3.1.6 Results of RIS at evolving cell walls

Under irradiation, the dislocation loop density within the interior of the dislocation cell and the network dislocation density at the cell walls of the AM microstructure co-evolve

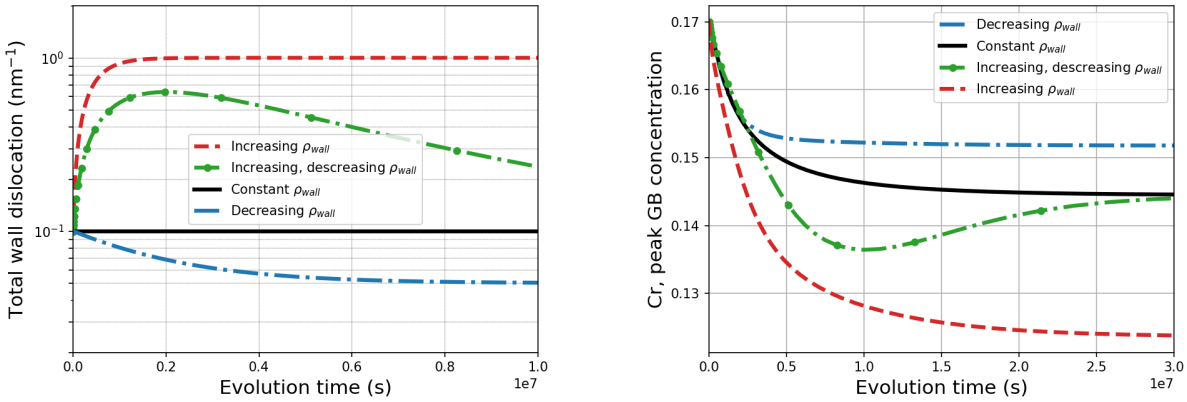

(a) (b)

Figure 21: (a) Time evolution of total dislocation density across cell wall ρ_{tot} realized using different functional forms for ρ_{wall}. (b) Cr concentration evolution at the center of cell wall for different dislocation density evolution in (a).

(Section 2, Refs. [10, 11, 40]). While quantitative data on dislocation evolution in the AM microstructure must be characterized in FY2024, the evolution of dislocation structures in cold-worked SS under irradiation has been a subject of extensive research [37, 41, 42]. To capture the various evolution trends, we employ mathematical functions based on exponentials and their distributions. We simulate ρ_{tot} across the cell wall using different functional forms, shown in Fig. 21a. Corresponding results of RIS evolution for Cr at the GB are shown in Fig. 21b. For the non-monotonically evolving ρ_{tot}, the Cr concentration decreases and then increases to a steady-state value. For both the constant and decreasing ρ_{tot}, the Cr concentration decreases, but to different steady-state values.

3.1.7 Results of RIS in AM microstructures

To simulate RIS in AM SS, we employ a representative 2D microstructure with hexagonal dislocation cells of 0.5 μm width within a square grain of 1×1 μm^2, as shown in Fig. 22b. The hexagonal cell structure in PF is stable against boundary movement and prevents evolution of the cells. Dirichlet boundary conditions $c_v = c_v^e$ are applied on the point defect concentrations along the edges of the square grain to describe the sink action of general HAGBs. For comparison, RIS simulations are also performed on an identical square grain GB system without dislocation cells as shown in Fig. 22a. The steady-state concentrations for point defects and atomic components are shown in Fig. 22c and d, respectively. The concentration of point defects at the cell walls are orders of magnitude greater than the ideal value of c_v^e at GB and at least an order of magnitude lower that that in the center of the dislocation cell. Lower RIS concentrations are observed at the cell walls compared to the GB due to their non-ideal point defect absorption characteristics. Moreover, RIS at GB in the AM microstructure is lower that that in the reference microstructure

due to the presence of the higher dislocation sink density within the grains in the former.

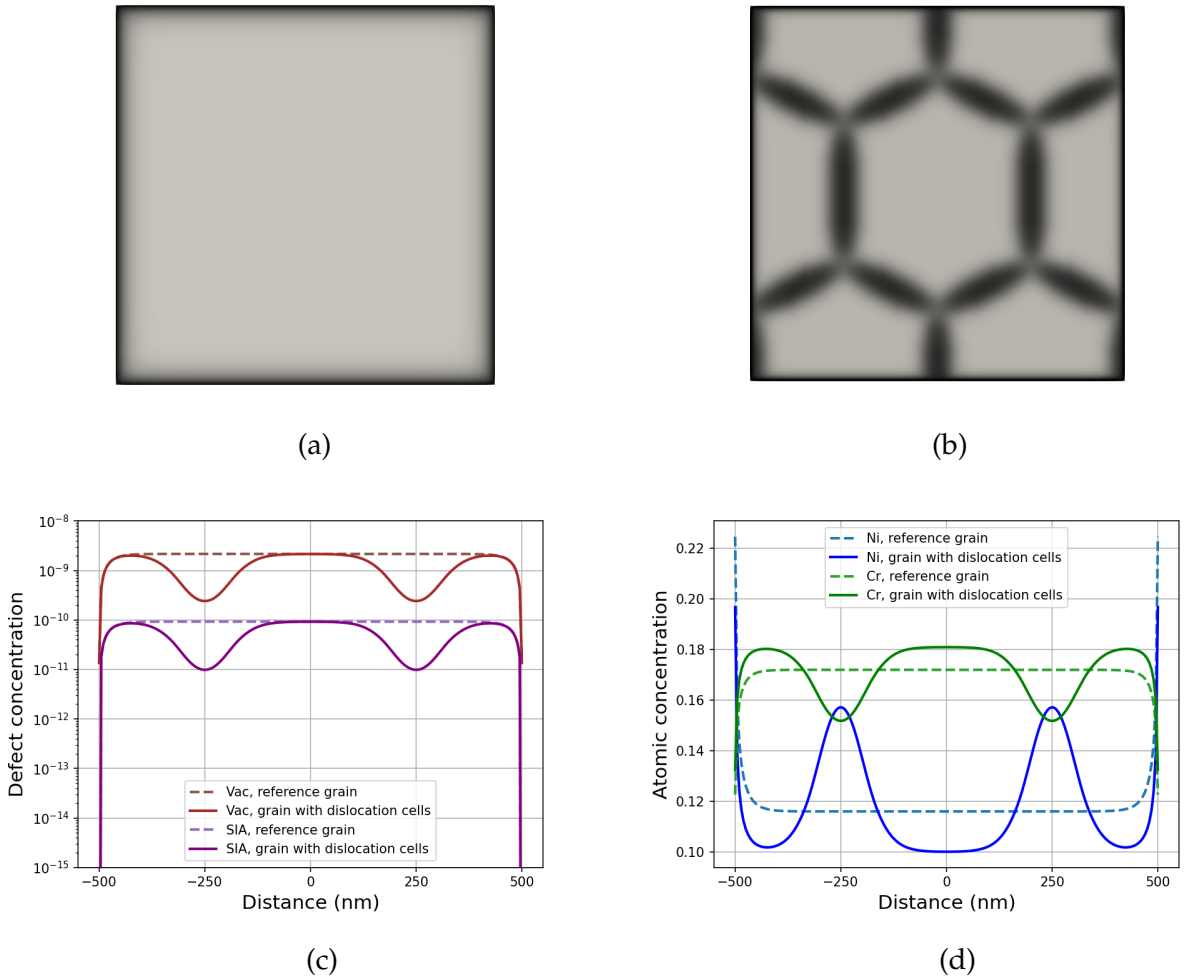

Figure 22: PF simulation of RIS in 2D. (a) Square grain of 1×1 μm^2 size with general HAGB at the edges (dark region) of the square domain. (b) Hexagonal dislocation cells walls (dark region) to form dislocation cells of 0.5 μm width within the square grain shown in (a). Line profiles of (c) point defect and (d) atomic concentrations at steady state are taken horizontally from the center of 2D domains in (a) and (b).

3.2 Molecular dynamics studies of radiation damage in 316 SS

3.2.1 Assessment of available interatomic potentials

Molecular dynamics (MD) is a technique for modeling the behavior of a system consisting of an ensemble of atomic particles using the classical Newtonian equations of motion. The motion of each atom in the simulation is tracked through time by determining the forces acting upon it using an interatomic potential and then numerically integrating in time to obtain its position at the next time step of the simulation. In this work, MD simulations were performed using the LAMMPS (Large scale Atomistic/Molecular Massively Parallel Simulator) software, an

open source package developed by Sandia National Laboratories [43] that is highly optimized for running MD simulations across many Central processing unit (CPU) and or Graphical processing unit (GPU) cores. To model the high energy collisions involved in collision cascades, these simulations need to account for the forces arising from a variety of physical phenomena, requiring the combination of several models to accurately represent the forces in the system.

The forces between two interacting particles are considered to be the most fundamental aspect of radiation damage, without which it is impossible to define microstructural properties and defect energetics. These forces are described by interatomic potentials, which are typically empirical functions created from fitting either density functional theory or experimental data. The accuracy of interatomic potentials is vital for the accuracy of simulation outcomes. Development of accurate interatomic potentials in extremely time-consuming and is generally focused on describing specific phenomena (e.g., melting, phase transitions, or radiation damage), and becomes more complicated as the number of elements in the potential increase. As a result, we cannot build an interatomic potential for radiation damage in 316 SS; instead, we must first assess the available interatomic potentials for fitness to the needs of this investigation while making reasonable simplifications to the composition space studied.

The forces modeled in this work can be broken down into three separate components. The first is long range forces, which we are modeling using potential models based on either embedded atom method (EAM) or Tersoff [44, 45] forms. Initial tests were performed on the EAM potential developed by Zhou et al. [46] to model Fe-Cr-Ni systems. However, it was found that the model had issues accurately modeling the vacancy formation energy in 316 stainless steel and maintaining the correct crystal structure when simulating collision cascades. Conversely, the model developed by Beland et al. [47] for modeling collision cascades in Fe-Cr-Ni systems was found to produce more realistic results. Additionally, a Tersoff model developed by Henriksson et al. [48] was used in order to study Fe-Cr-C systems to investigate the effect of carbon content on collision cascades and the diffusion of point defects. The second type of forces are short range forces resulting from screened nuclear repulsion. These are modeled using the universal Ziegler, Biersack, and Littmark (ZBL) potential [49] appended to the long-range forces described by EAM or Tersoff models. The last force component is an electronic stopping model that accounts for the inelastic energy loss of fast moving atoms in solids due to electronic collisions [50, 51]. The strength of the electronic stopping power in each material was calculated using the Stopping and Range of Ions in Matter program (SRIM) [52]. An alternative method is the two-temperature model that provides a more detailed accounting of energy transfer between the electronic and ionic systems; however, this is a quite burdensome method to parameterize involving many density functional theory calculations, which is particularly challenging for elements with unpaired electrons (i.e., Fe, Cr, and Ni in 316 SS). The electronic stopping method is a commonly accepted method to include electronic stopping within molecular dynamics simulations.

3.2.2 Partial diffusivity simulation methods

Measuring diffusivity of point defects in an alloy using MD raises a few complications over a pure material. The standard method for measuring the diffusivity of vacancies or interstitials in a pure material is to create an MD simulation with a single defect. This avoids the difficulty of tracking the position of the vacancy or SIA through time, because all change in the mean square displacement (MSD) can be attributed to the presence of a defect. From this point the diffusivity can be calculated using the Einstein relation:

$$D = \frac{r_s^2(t)}{2nt} \tag{16}$$

where $r_s^2(t)$ is the MSD of the object, t is time, and n is the dimensionality of the system. In this case the object would be all of the atoms in the simulation, and the corresponding result is the tracer or defect diffusion coefficient, respectively.

In alloy systems this becomes more complicated, because there is a need to determine the partial diffusivity of vacancies and interstitials in the system. This means that, for each defect type, we need to determine both the diffusion rate of the defect due to each of the constituent elements in the alloy, but also the diffusion rate of each of the constituent elements due to the point defect. The diffusion of the defect due to each constituent element can be calculated by calculating the MSD of each element separately instead of for all atoms in the system. Additionally, a set of reference simulations without any defects provide a baseline measure of any diffusion that might occur in the simulation that is unrelated to the presence of a point defect. Using these defect partial diffusivities, the composition of the alloy, and the average SIA formation energies for each SIA type, the diffusion rate of each species due to the presence of a vacancy or an interstitial can be calculated [1]. Note that the SIA formation energies are needed to adjust the diffusion calculations to account for the preferential atom-interstitial binding, e.g., the likelihood of the SIA being of each species at any point in time.

Periodic computational cells are employed to represent bulk material systems. To capture the defect MSD, a single defect (either a vacancy or an SIA) is introduced into a simulation box of $15 \times 15 \times 15$ unit cells containing approximately 11,000 atoms. This size was chosen as the smallest simulation domain that could be used without causing the point defect diffusion rates to change as a result of self-interaction. The MSD was measured in increments of 10 ps for a total of 1 ns per simulation. Simulations were repeated a minimum of 20 times or until a sufficient quantity of data was collected to accurately measure the defect diffusivities.

3.2.3 Collision cascade simulation methods

To model the development of a collision cascade and its subsequent defect recombination process, we use a large simulation box with periodic boundary conditions. A simulation with a supercell size of $70 \times 70 \times 70$ unit cells was found to be sufficient to contain all of the displaced atoms within the computational domain, avoiding the spurious effects of cascade self-interaction

with periodic boundary conditions. The typical lattice for each metal type was then generated in the simulation box, and the simulation was then equilibrated for 50 ps at temperature of 300 K and 1 bar using a Nosé–Hoover thermostat and barostat [53, 54].

The collision cascade simulations are performed using a primary knock-on atom (PKA) that has an initial energy within the range of 1 keV and 15 keV. The displacement cascades are initiated by choosing a random atom near the center of the computational domain as the PKA. The PKA was then assigned a velocity corresponding to the desired initial PKA energy in a random direction. To capture the cascade propagation with the correct dynamics, the time step size is adjusted at different stages of the cascade propagation. During the ballistic phase, a time step of 0.01 fs is used to simulate the collision cascade for the first 1.5 ps of the cascade. As the kinetic energy of the displaced atoms is transferred to other atoms and dissipated in the system, the velocity of the displaced atoms decreases and the time step is increased to 0.1 fs until 6.5 ps, and finally the time step is increased to 1 fs for the rest of the simulation. The cascade simulations are run to 200 ps to achieve a steady state in the number of remaining defects. It should be noted that the cascades generated in this work produce most of the basic physical phenomena of primary radiation damage. To remove the bias of the initial PKA direction on the collision cascades simulations, the simulations were repeated in 10 random directions for each test condition unless otherwise specified. To remove the excess heat produced from the gradual dissipation of the applied kinetic energy, a Nosé–Hoover thermostat is applied far away from the collision cascade. This thermostat is used to keep atoms within 1 unit cell of the edges of the simulation domain at a temperature of 300 K. At the end of the simulation, the average temperature of the entire system has returned to the initial value. The identification of defects, including visualization, quantification, and categorization, is carried out using the Wigner-Seitz method [51], which is implemented both in LAMMPS and within the visualization tool OVITO [55]. The Wigner-Seitz method compares the crystal structure of the irradiated material system with a non-irradiated equilibrated material as the reference structure. The number and location of defects is calculated every 1000 time steps.

3.2.4 Results of partial diffusivity studies

MD simulations were performed to measure the partial diffusivities associated with point defects in 316 SS. This was done by modeling randomized fcc lattices with material compositions similar to that of 316 SS inside of an MD simulation. A single point defect was created, and the resulting MSD was tracked over time for each species of atom. The excess MSD relative to a reference simulation with no defects was then used to calculate the diffusion rate of each component and calculate the diffusion rate of the defect as a result of each atom species.

Initially, the simulations to measure partial diffusivity were performed using an Fe-Cr-Ni alloy, using the Béland potential [47], as a model for 316 SS. Partial diffusivities were successfully calculated for both vacancies and SIAs; however, there were obvious discrepancies between the obtained diffusion rates and tracer diffusion studies in the existing literature. Most significantly,

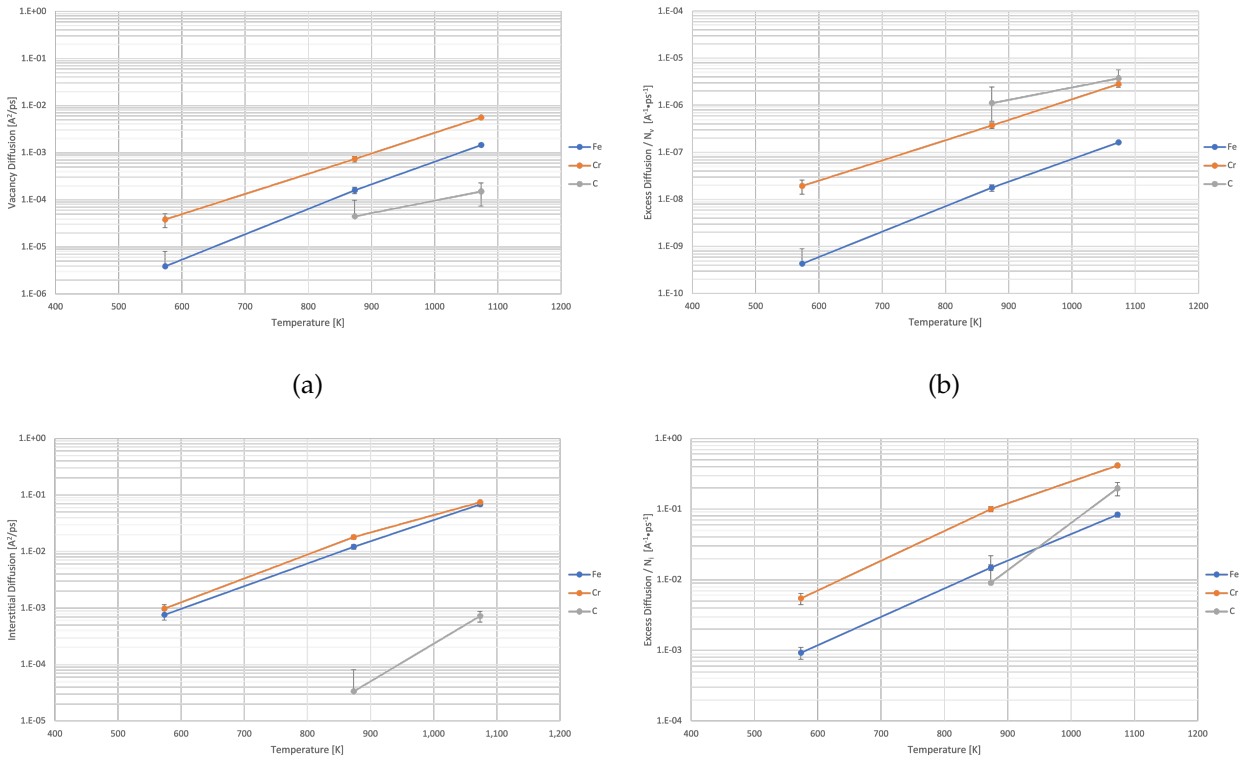

Figure 23: Diffusion measurements of point defects in a Fe-Cr-C alloy modeling 316 SS. a) Partial diffusivity of vacancies due to each component species. b) Partial diffusivity of each component species due to vacancies, relative to the concentration of vacancies. c) Partial diffusivity of interstitials due to each component species. d) Partial diffusivity of each component species due to the interstitials, relative to the concentration of interstitials.

the MD simulations indicated that Ni was the fastest diffusing element, followed by Fe, and then Cr. This stands in contrast to experimental results which indicate that Cr should be the fastest diffusing, followed by Fe, and then Ni [56]. Due to the issues using this model to represent the diffusion properties of 316 SS, it was set aside in favor of modeling 316 SS with the force field model created by Henrkisson et al. [48].

Simulations studying the diffusion of vacancies and SIA in the Fe-Cr-C system were performed for a material composition of 18 wt% Cr, 0.08 wt% C, and the balance Fe. The diffusion simulations were performed for equilibrated systems with temperatures of 300°C, 600°C, and 800°C. The excess diffusion resulting from the introduction of a vacancy is shown in Figure 23a. From these results we can see that Cr atoms contribute the most to the diffusion of vacancies in the material, 10-20 times more so than iron atoms. Also note that carbon atoms had an negligible contribution to the diffusion of the vacancy, and their contribution to excess diffusion was undetectable at 300°C. This raises the possibility that the presence of carbon interstitials could be slowing the diffusion of individual vacancies (e.g. carbon-vacancy trapping).

Using the measured diffusivity of the vacancy and the composition of the model material, we can also calculate the diffusion of the atoms due to the presence of the vacancy, shown in Figure 23b. One of the interesting results of presenting the data in this manner is that it highlights that even though the carbon does not have a major impact on the diffusion of the vacancy, the presence of the vacancy increases the diffusion of carbon similarly to the increase in diffusion of iron atoms.

Similar simulations were performed to measure the diffusion of an interstitial. Starting from the same model material, an iron SIA was added to the simulation and the resulting diffusion was tracked. From the results shown in Figure 23c we find that both iron and chromium atoms contribute a similar amount to the diffusion of an interstitial, with the Cr atoms contributing slightly more than half of the total diffusion at lower temperatures. We also used this data to calculate the excess diffusion of each atom species due to the presence of the interstitial, shown in Figure 23d. There is qualitative agreement between these measurements and the experimental tracer diffusion studies [56] that the diffusion of Cr in response to created interstitials is several times faster than that of Fe atoms.

3.2.5 Results of modeling collision cascades in Fe-Cr-Ni

Collision cascade simulations allow us to study the production and annihilation of defects at different stages of the displacement damage cascade. The initial work investigating the development of collision cascades in 316 stainless steel was done by modeling a randomized fcc alloy composed of 71 wt%Fe, 18 wt%Cr, and 11 wt%Ni modeled using the Béland 2017 potential [47] at 300 °C. Figure 24 traces the production and annihilation of the defects at different steps of the displacement cascade and the variation in the cascade size based on the initial kinetic energy of the PKA. As can be observed from the time evolution of the cascade, the maximum size of the cascade has a non-linear relationship with the initial PKA energy. Additionally, the

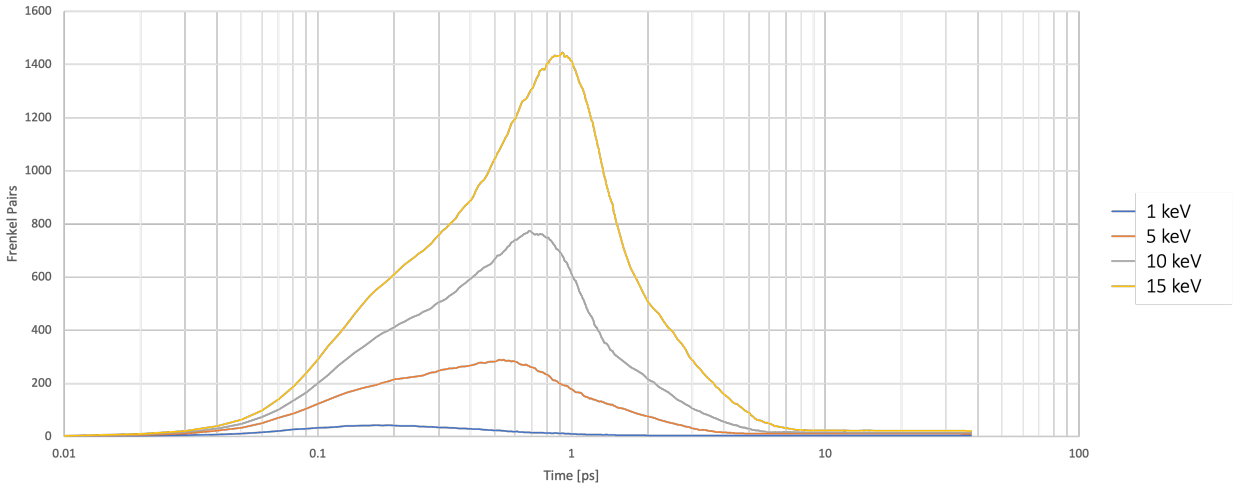

Figure 24: The average time evolution of cascade-created Frenkel pairs for an fcc system of 71 wt% Fe, 18 wt% Cr, and 11 wt% Ni at 1, 5, 10, and 15 keV PKA energy with an initial temperature of 300 °C. Each profile is the average of 10 collision cascade simulations.

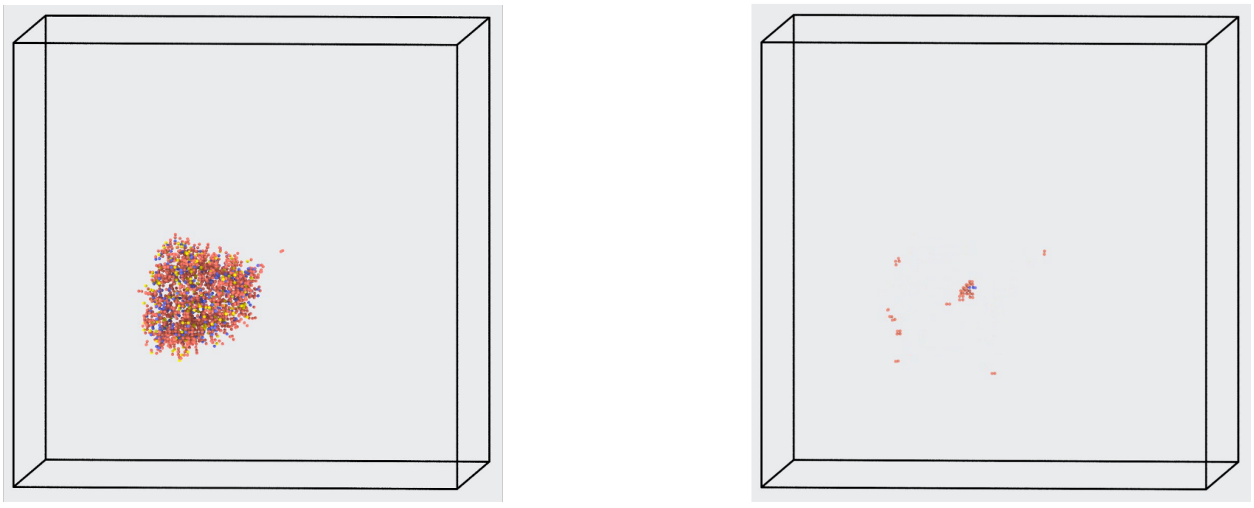

(a) (b)

Figure 25: Distribution of interstitials in Fe-Cr-Ni for a 15 keV collision at 300 °C. (a) Distribution of interstitials at the peak of the cascade (b) Distribution of interstitials after recombination.

time at which the cascade peak occurs is also dependent on the initial PKA energy, with 1 keV collisions peaking after approximately 0.2 ps and 15 keV simulations taking approximately 1 ps to reach their maximum size. Eventually the defect concentration reaches a quasi-steady-state concentration for times approximately $\geq$ 10 ps. The PKA simulations are carried out until a quasi-steady-state defect concentration is achieved. At the end of each cascade simulation, we observed a homogeneous temperature.

In addition to tracing the progression of collision cascades by counting the number of Frenkel pairs throughout the duration of the simulation, the Wigner-Seitz method also enables the visualization of defects to obtain qualitative data about the distribution of defects and determine if and when defect clusters begin forming during the recombination of defects. Figure 25 shows examples of the distribution of interstitial dumbbells captured during during the peak of a collision cascade as well as at the end of the simulation. As can be seen from Figures 24 and 25, there are very few Frenkel pairs that survive the recombination process using our model Fe-Cr-Ni system. In our simulations using EAM potentials to model long range forces, we found that the surviving fraction to be in the range of 2% to 8%. In general, we expect the fraction of surviving defects to be approximately 30% [1, 57], which calls into question the ability of EAM based force field models to accurately represent the recombination process.

3.2.6 Results of modeling the effect of carbon on collision cascades in Fe-Cr-C

Motivated by studies of carbon-vacancy trapping in α-iron [58, 59], we hypothesized that carbon could significantly affect radiation-driven microstructure evolution in 316H versus 316L, work began on a simulation campaign to determine how modifying the carbon percentage would effect the development of collision cascades and the subsequent recombination of defects. In order to model the impact of carbon, the Henriksson 2013 potential [48] was used for an Fe-Cr-C alloy with an fcc structure. Stainless steel was modeled as a randomized fcc lattice with 71 wt% Fe and 18 wt% Cr. Nickel was removed from this study because no potential exists to date that includes Fe-Cr-Ni-C. The number of carbons inserted into interstitial sites was modified to achieve the desired carbon percentage. After carbon atoms were inserted into the fcc structure, an energy minimization routine was run before equilibration.

Collision cascade simulations were run on randomized Fe-Cr-C alloys with carbon percentages varying between 0.0 wt%C and 0.1 wt%C to cover the full range of possible carbon content that could be expected out of AM 316 stainless steel. The simulations were run with an initial PKA energy of 15 keV and were repeated 20 times for each carbon composition. As with the previous collision cascade simulations performed for the Fe-Cr-Ni system, the cascade profiles shown in Figure 26 reach their peak size after approximately 1 ps. This is then followed by a period of defect recombination that lasts until approximately 20 ps after the start of the collision cascade. Unlike the cascades performed using an EAM based force field model, the cascades performed using the Henriksson model show a slow increase in the number of defects after the end of the recombination process.

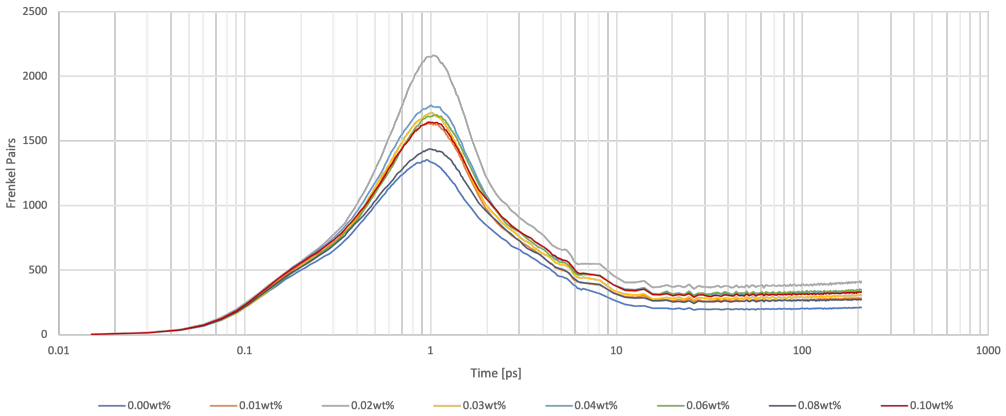

(a) 300°C

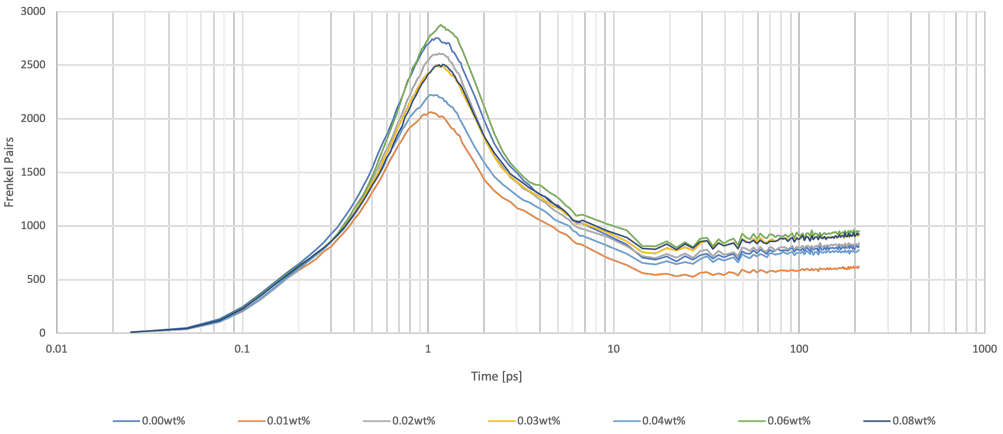

(b) 600°C

Figure 26: The average time evolution of 15 keV collision cascade for a random fcc crystal with 71 wt% Fe, 18 wt% Cr, and variable carbon content.

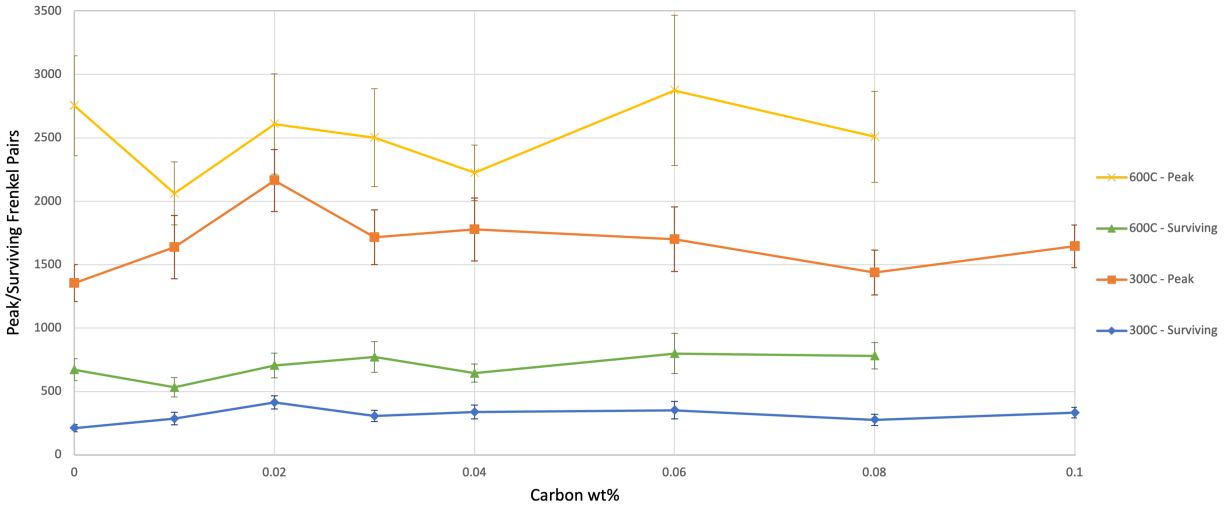

Figure 27: The average peak and surviving number of Frankel pairs for 15 keV collision cascade for a random fcc crystal with 71 wt% Fe, 18 wt% Cr, and variable carbon content.

We can see from the collision cascade data shown in Figure 27 that the amount of carbon in the stainless steel has a significant impact on both the maximum size of the collision cascade as well as the number of surviving Frenkel pairs. This is particularly apparent in the simulations run at 300 °C, where our model 316 SS shows that increasing carbon content from 0.0 wt% to 0.02 wt% results in the peak cascade size increasing to a maximum of 2164 Frenkel pairs. The size of the cascade then reduces for models containing higher percentages of carbon. However, we can also observe from Figure 27 that the effect is diminished at higher equilibrium temperatures. This temperature dependence suggests that it is the carbon content's effect on the material properties of stainless steel which is causing the change in size of the collision cascades, rather than the carbon interstitials having a direct influence on the progression of the collision cascade.

Unlike the EAM model used for the Fe-Cr-Ni system in the previous section, the MD potential used to model the Fe-Cr-C system is based on a more complex Tersoff style potential. This change results in a very different outcome when modeling the recombination of the cascade. As seen in Figure 27, we find a significantly higher percentage of surviving Frenkel pairs. Where as the EAM style potential predicted that $\leq$ 8% of the defects would survive recombination, the Tersoff style potential predicts that 15% - 25% of defects will survive at 300°C and 24%-31% will survive at 600°C. This result is in closer agreement with the expected 30% fraction of surviving defects. It is also important to note that the percent of surviving defects was relatively consistent across carbon contents, and that the differences where within the margin of error for our measurements. This implies that the peak number defects created in the collision cascade has a major influence over the total number of surviving Frenkel pairs generated by the collision cascade.

In another difference from the results in Section 3.2.5, we can observe the number of defects detected via the Wigner-Seitz method slowly increasing for simulation times greater than 20 ps. This increase corresponds to the formation of interstitial clusters and the merger of those small

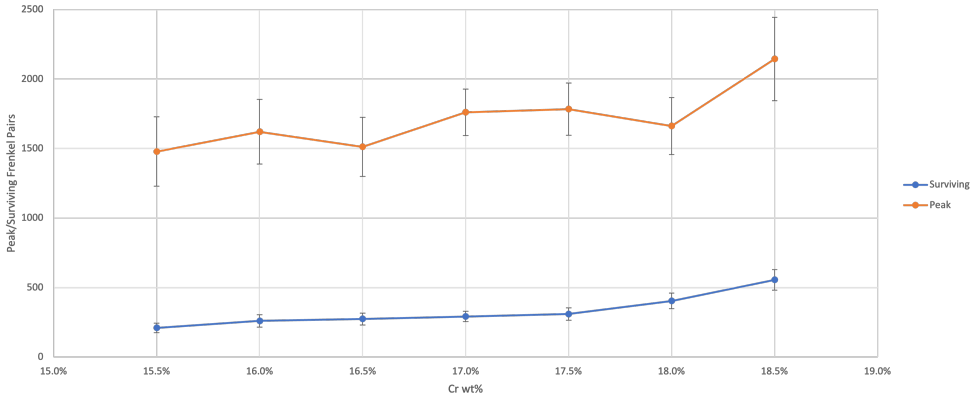

(a)

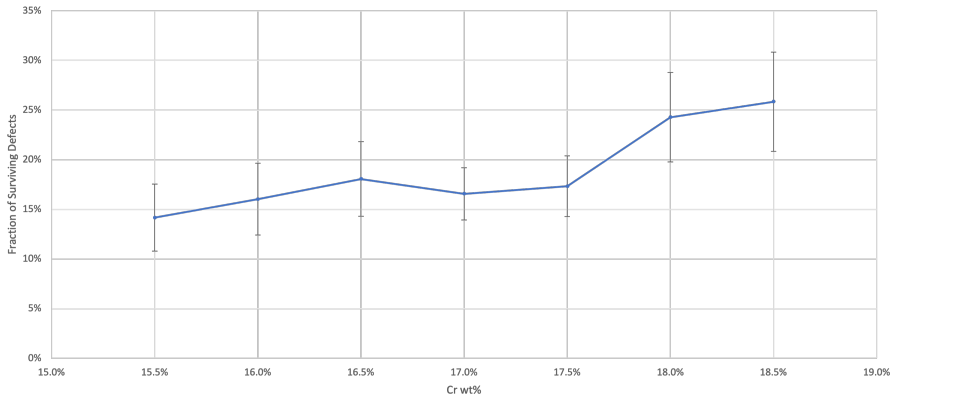

(b)

Figure 28: The (a) average peak and surviving number of Frankel pairs and (b) surviving fraction of defects for 15 keV collision cascade for model 316 SS with 0.08wt%C and variable chromium content at 300°C.

clusters into larger ones. Our current hypothesis is that the diffusion of these defects clusters towards each-other is trapping a small number of atoms on fcc sites between the clusters and causing them to become displaced. If this is indeed the case, we should expect the increase in number of defects to taper off at longer timescales.

3.2.7 Results of modeling the effect of chromium on collision cascades in Fe-Cr-C

In addition to looking at what effects the variation in carbon content could have on the irradiation behavior of AM-316, we also investigated what impact the variation of chromium content could have on defect generation, based on the variation in chromium seen in samples of AM-316. To perform this investigation, collision cascade simulations were performed with randomized fcc lattices containing variable amounts of Cr atoms. Carbon atoms were added to interstitial sites to bring the carbon content up to 0.08 wt% carbon. 15 keV collision cascade simulations at 300°C were performed on randomized Fe-Cr-C alloys with chromium percentages varying between 15.5 wt%Cr and 18.5 wt%Cr to cover the full range of possible chromium

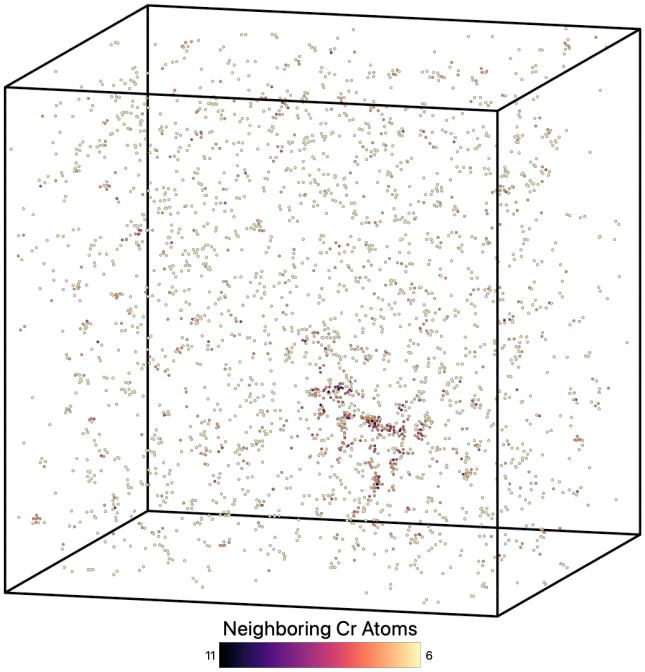

Figure 29: Distribution of Cr atoms colored according to the number of neighboring Cr atoms in a Fe-Cr-C alloy after a 15 keV collision cascade. Cr atoms with 5 or less neighbors are not shown.

content.

The results from the collision cascade simulations show that for chromium content less than 18.5 wt%, there is no significant difference in terms of the peak size of the collision cascade. However, the number of surviving Frenkel pairs consistently increases with rising chromium content. Unlike changing the carbon content in the model 316 SS, we can observe from the data in Figure 28b that increasing the chromium content in the model 316 SS generally results in an increase in the fraction of defects that survive the recombination process.

In observing the distribution of defects after the collision cascade, it was observed that there is significant segregation of iron and chromium atoms at the end of the recombination process. An example of this segregation is shown in Figure 29. This behavior is not entirely unexpected, since a similar phenomena has previously been observed in ferritic and martensitic steels [60]. Based on the timing of when the segregation occurs (as the cascade is reforming the fcc lattice), we hypothesize that this segregation is due to the difference in melting points between iron and chromium.

The segregation of iron and chromium atoms during the recombination process provides a possible explanation for the mechanism by which the fraction of surviving defects increases as the chromium content of the model material also increases. However, determining the validity of this hypothesis will require additional work.

4. Discussion

In fiscal year 2023, we have studied the radiation-driven microstructural evolution of LPBF 316 material bearing both the 316L and 316H specifications. Being a new material (as defined by the novel manufacturing method), experimental investigations are necessary to reveal the behavior of the material under irradiation. Ion irradiation is a very useful tool for accelerated irradiation effects testing, especially for understanding microstructural evolution, which underpins structure-property relationships. These experimental results provide information about starting microstructure and radiation-induced microstructure evolution and motivates questions to the modeling effort, which aims to develop the ability to model radiation-driven microstructural evolution in additively-manufactured 316 stainless steel under a variety of advanced reactor conditions, including different temperatures, neutron spectra, and fluxes, in a sort of "virtual experiment".

Pre-irradiation characterization of the LPBF 316L and LPBF 316H specimens revealed similar microstructures regardless of the machine the specimens were printed with and the specific chemical compositions of the specimens. The specimens had relatively large differences in the amount of nitrogen, carbon, chromium, and manganese, although the 316H specimen was only slightly over the lower limit the 316H carbon specification. The LPBF 316L-2 specimen was near the upper limit of the nitrogen specification; nitrogen acts in a similar fashion in many ways to carbon in austenitic steel in terms of interstitial solid solution strengthening and precipitation of chromium compounds at high temperatures. The specimens all had a cellular substructure within relatively wavy high-angle grain boundaries. The cells were columnar in nature, with a radius of approximately 500 nm and the cell walls composed of tangled network dislocation walls of approximately 50 - 100 nm in width. The interior of the cells were largely free of dislocations. The cell walls were decorated with (Si, Mn) oxides with an average radius of approximately 20 nm. Microchemical segregation was present at the cell walls, but not at the high angle grain boundaries. The cells walls were enriched in Cr, Mo, and Ni, and depleted in Fe. Large (roughly 1 μm) inclusions were occasionally present. Ion irradiations of LPBF 316L and LPBF 316H were performed both *in-situ* (i.e., simultaneous ion irradiation and imaging of a TEM foil) and *ex-situ* (i.e., ion irradiation of a thick specimen that is characterized after irradiation). *In-situ* ion irradiation is beneficial because characterization at multiple doses is possible for a single specimen; in addition, kinetic properties can be measured. However, *in-situ* irradiation behavior is affected by the thickness of the foil at the irradiation location. The foil surfaces act as sinks for irradiation-induced defects; the separation distance between the surfaces (sinks) affects the concentration of defects that are available within the bulk to form radiation-induced features such as dislocation loops. *Ex-situ* ion irradiation requires more time to characterize, but it is not subject to the same issue of foil thickness affecting the development of irradiation-driven microstructures, although it is still necessary to know the sample thickness when performing analysis of TEM data. It can also provide information on a larger volume of material, such as nanohardness measurements.

All three LPBF 316 compositions showed similar behavior during *in-situ* ion irradiation with 1 MeV Kr^{2+} at 300 °C or 600 °C. For the irradiation at 300 °C, a high density of small dislocation loops formed quickly at low doses and were uniformly distributed within the preexisting dislocation cells, including the cell walls; the dislocation cell structure did not significantly affect the spatial distribution of dislocation loops. At high doses, extended dislocation structures were formed due to the coalescence of dislocation loops. Although the loop populations can be characterized in terms of number and size as they evolve with dose, quantitative analysis and comparison requires the foil thickness, which will be characterized in fiscal year 2024. For the irradiations at 600 °C, a few faulted and perfect dislocation loops were formed initially at the centers of the dislocation cells. With increasing dose, the loops grew and gradually populated the entire area of the dislocation cells, including the cell walls. At high doses, the initial dislocation cell structure was replaced by network dislocations.

The phenomenon of RIS was observed in LPBF 316H irradiated at 600°C. Interestingly, RIS occurred at high angle grain boundaries (which were initially uniform in composition), but the initial microchemical segregation at the dislocation cell walls was generally left mostly unchanged. At the high-angle grain boundaries, Si, Ni and O were enriched after irradiation, while Mn and Cr were depleted. The Cr, Ni and Mo enrichments and Fe depletion at the cell walls were still visible after irradiation, but the extents may have been reduced. These results indicate that the sink strength of the dislocation cell walls is much less than that of the high angle grain boundaries. In addition, the existing Cr enrichment at the cell walls was replaced with dense Cr-rich oxide nanoparticles. These Cr-rich oxides were not observed in the sample exposed to the same temperature without irradiation, indicating that they are a radiation-driven precipitation. This may have been driven by oxygen enrichment at the dislocation cells or purely by radiation-induced precipitation; however, the formation of chromium-rich oxides is likely to degrade the corrosion resistance of the irradiated material by reducing the availability of chromium in solution to form a continuous chromium-oxide passivating film on the surface of the material.

Ex-situ ion irradiation were performed on LPBF 316L SS at 600°C and 300 °C with 4 MeV Ni ions at three dose rates, 10^{-3} dpa/s (up to 10 dpa), 10^{-4} dpa/s (up to 2 dpa), and 10^{-5} dpa/s (up to 0.2 dpa). The results of nanoindentation tests performed on the 600°C LPBF 316L-1 samples showed a complex dose dependence, with the sample softening at 2 dpa, but hardening at 5 dpa and further hardening at 10 dpa. This result appears to qualitatively correspond with the observed radiation-driven microstructure evolution of the LPBF 316 specimens: initially, the dislocation cell walls narrow, indicating recovery of the dislocation network, which would lead to softening; further irradiation produces dislocation loops and loop unfaulting into network dislocations, which would drive increasing hardening behavior. This behavior is similar to that observed in cold-worked austenitic stainless steels.

The experimental data provided motivated the modeling investigations at the mesoscale and atomistic scale. At the mesoscale, the modeling team developed a novel phase field model for

radiation-induced segregation in additively manufactured materials. Previous phase field models have been created to handle grain boundaries, but a new formulation had to be developed to handle the diffuse dislocation cell wall structure within high angle grains along with the migration of not only chemical solute species, but also vacancies and interstitials. With the development of this model, we are positioned to quantitatively study radiation-induced segregation in additively manufactured 316 stainless steel in fiscal year 2024. The model can be extended to include the density of nanoscale sinks found in additively manufactured material, such as the nanoscale oxides present from the additive manufacturing build process as well as the precipitation of chromium oxide precipitates under irradiation. It can also be linked to a cluster dynamics model for the evolution of the dislocation loop population.

The mesoscale phase field model for RIS in AM microstructures was developed for a representative Fe–Ni–Cr ternary alloy using the MOOSE/Marmot framework. Physically realistic grain boundary and dislocation cell widths are achievable. While the ion irradiation experiments were ongoing, the phase field model was exercised to understand the impact of certain model parameters on the predicted phenomena. The steady-state concentration profiles for vacancies, interstitials, chromium, and nickel at high-angle grain boundaries was assessed for the physical behavior and the diffuse interface width (and therefore necessary mesh resolution) needed to converge the results; chromium depletion and nickel enrichment at grain boundaries was observed, in agreement with experimental observations, and the nickel concentration within the dislocation cell was most sensitive to the choice of interface width.

We find that the experimentally observed differences in RIS behavior at grain boundaries versus dislocation cells can be explained due to their different defect sink characteristics. We find that the width of the area exhibiting RIS is directly proportional to the width of the dislocation cell wall and the maximum depletion or enhancement of concentration is directly proportional to the dislocation density. Importantly, we find that the dislocation cell wall exhibits much less RIS than the high angle grain boundary, which is in agreement with the experimental observations discussed previously. We also examined the effect of grain boundary misorientation on the sink strength of the grain boundary and thus its effect on steady-state concentration profiles in RIS. We find that low angle grain boundaries (less than approximately 4°) do not exhibit RIS, while the maximum steady-state concentration achieved during RIS saturates at approximately 21°and greater. These results could potentially explain the difference in grain boundary RIS observed from ion irradiation, and could also be used to predict the RIS behavior of an additively-manufactured material given its specific distribution of grain boundary angles and dislocation cell characteristics.

We also find that the degree of RIS at a high angle grain boundary has a temperature dependence and exhibits a maximum at intermediate temperatures. This is tied both to the far-field concentration of defects away from the grain boundary as well as the difference in defect concentration between the grain boundary and the far-field; the greater mobility of defects at high temperatures will prevent the formation of concentration gradients, while low defect

mobility will prevent significant flux and RIS development. Dose rates also affect the degree of RIS, with higher dose rates (representative of ion irradiations) accelerating RIS, increasing the maximum concentration difference versus the nominal concentration, and shifting it to higher temperatures versus lower dose rates (e.g., neutron irradiations). The effect of the time evolution of the density of dislocations within cell walls was also studied, and we find that a decreasing dislocation density within the walls will result in limited RIS initially that self-limits with only a few percent change in concentration. Other evolutions of the density will result in other RIS behavior; supplied with experimental information about dislocation density evolution within the cell walls, quantitative predictions of RIS can be made.

With better informed input from lower length scale atomistic or rate theory simulations, the phase field model can be parameterized more physically in the future to yield more accurate predictions. We performed molecular dynamics studies of the creation and diffusion of defects at the atomistic level in order to address some of these needs. We begun by assessing the behavior of various interatomic potentials, which is a necessary first step to obtaining physically realistic values for the quantities of interest. As of today, no one interatomic potential is available that models the Fe-Cr-Ni-C system; the two best available interatomic potentials lack either Ni or C. Developing an interatomic potential is a time-consuming process outside of the scope of this project; therefore, we must make reasonable simplifications when needed. We found that the Henriksson interatomic potential for Fe-Cr-C is able to qualitatively reproduce the partial diffusivities of the Fe-Cr-C system with reasonable accuracy. This makes it possible to study a number of important phenomena, such as carbon-vacancy trapping, the sink strength and diffusion rates of defect loops and clusters, and the sink strengths of grain boundaries, which will be studied next fiscal year and are important parameters for modeling microstructure evolution (e.g., dislocation loop formation and growth, radiation-induced segregation).

Accurate predictions of collision cascade processes are necessary for modeling radiation damage in materials, including the peak number of defects formed during the cascade and the characteristics of the surviving defect population after the defect recombination phase. The surviving defect population (vacancies, interstitials, various vacancy clusters, various interstitial clusters, etc.) are particularly important for microstructure evolution on diffusive timescales. We found that an embedded-atom-method interatomic potential of Fe-Ni-Cr produces very few surviving surviving defects, which is unrealistic. We hypothesize that the isotropic nature of that potential allows for too much defect recombination within a crystal structure; the directional Tersoff potential for the Fe-Cr-C system produces much more realistic surviving defect fractions.

Motivated by studies of carbon-vacancy trapping effects in bcc iron, we hypothesized that carbon content could affect the behavior of collision cascades in 316 stainless steel. We performed collision cascade simulations in fcc Fe-Cr-C with carbon varying from 0 wt% to 0.08 wt% at 300 °C and 600 °C. First, we found that the peak number of defects (measuring the extent of the cascade) and the final number of surviving defects were greater at 600 °C than at 300 °C for all carbon contents. Trends with respect to carbon content at each temperature are harder to discern. It

does appear that the maximum cascade size and surviving defect population is affected by carbon content, especially at 300 °C, but the effect is diminished at 600 °C. Therefore, any effect of carbon content on radiation-driven microstructure evolution is likely due to the effect of carbon on other material properties, and not directly a result of collision cascade behavior.

Motivated by the experimental observations of radiation-induced segregation, we also studied the effect of variable chromium content on collision cascade behavior, hypothesizing that there could be a feedback effect between radiation-induced segregation and further irradiation damage behavior. We studied an Fe-Cr-C system with chromium varying between 15.5 wt% and 18.5% and found a consistent trend that higher chromium contents lead to larger collision cascades and higher numbers of surviving defects and greater surviving defect fractions. This may be due to the segregation of iron and chromium atoms; additional work is necessary to quantify the segregation of elements and determine if this is indeed the cause. Chromium clustering may be a cause of the experimentally observed Cr-rich oxide nanorods within the additively manufactured material. In addition, because chromium depletion at grain boundaries is tied to the flux of vacancies to sinks, less production of defects at Cr-depleted regions will affect RIS behavior, possibly in a complex fashion. This information can be incorporated into the phase field model of RIS.

5. Conclusions

In conclusion, we have investigated the radiation damage behavior of additively-manufactured 316 stainless steel with a combination of ion irradiation and computational modeling. We aimed to understand how the unique microstructure as well as the variability affected the radiation damage behavior; variability arises in the processing conditions as well as the composition (macroscale heat variations and microscale heterogeneity). We found that processing conditions did not make significant impact on the as-built microstructure or compositional micro-heterogeneity. We did find that AM microstructures do have characteristic differences from conventional wrought material, including dispersed populations of nanoscale oxides and dislocation cells with microsegregation. We found that radiation-induced segregation behavior is much stronger for high-angle grain boundaries versus for the dislocation cell walls, which is driven by the much higher sink strength and the much narrower width of a high angle grain boundary versus a dislocation cell wall. In addition, we find that temperature has a significant impact on the microstructure evolution; irradiation at 300 °C results in a large population of small, uniformly distributed dislocation loops that ultimately merge into network dislocations, while irradiation at 600 °C results in a smaller population of larger dislocation loops that form within the dislocation cells (that also eventually form network dislocations). Further characterization is required to quantify the effect of composition on microstructure evolution under irradiation at each temperature; however, atomistic studies indicate that any effect of carbon content on radiation damage behavior would likely arise not from direct alteration of collision cascade behavior but rather its impact on diffusive processes and properties. However, chromium content does appear to be directly proportional to the collision cascade size and the number of defects that survive the initial recombination phase, which may feed back into RIS behavior.

Further experimental characterization and modeling will shed light on the effect of temperature on radiation-driven microstructure evolution in additively manufactured materials as well as the sensitivity of this microstructure evolution on process and compositional variability. This work positions the AMMT program strongly for the parallel investigations into the behavior of the material under neutron irradiation and its ultimate goal of being able to use a combination of ion irradiation and neutron irradiation for accelerated testing and qualification of materials for deployment in nuclear reactors.

REFERENCES

[1] G. S. Was, Fundamentals of radiation materials science : metals and alloys, second edition Edition, Springer, New York, 2017.

[2] R. Averback, T. de la Rubia, Displacement damage in irradiated metals and semiconductors, Solid State Physics - Advances in Research and Applications 51 (C) (1997) 281–402. doi:10.1016/S0081-1947(08)60193-9.

[3] K. Arakawa, K. Ono, M. Isshiki, K. Mimura, M. Uchikoshi, H. Mori, Observation of the one-dimensional diffusion of nanometer-sized dislocation loops, Science 318 (5852) (2007) 956–959. arXiv:https://www.science.org/doi/pdf/10.1126/science.1145386, doi:10.1126/science.1145386.
URL https://www.science.org/doi/abs/10.1126/science.1145386

[4] W. Xu, Y. Zhang, G. Cheng, W. Jian, P. C. Millett, C. C. Koch, S. N. Mathaudhu, Y. Zhu, In-situ atomic-scale observation of irradiation-induced void formation, Nature Communications 4 (1) (2013) 2288. doi:10.1038/ncomms3288.
URL https://doi.org/10.1038/ncomms3288

[5] M. R. Tonks, D. Gaston, P. C. Millett, D. Andrs, P. Talbot, An object-oriented finite element framework for multiphysics phase field simulations, Computational Materials Science 51 (1) (2012) 20–29.

[6] C. J. Permann, A. M. Jokisaari, M. R. Tonks, D. Schwen, D. R. Gaston, F. Kong, R. Hiromoto, R. C. Martineau, Scalable feature tracking for finite element meshes demonstrated with a novel phase-field grain subdivision model, Nuclear Technology 207 (7) (2021) 885–904.

[7] D. Schwen, L. K. Aagesen, J. W. Peterson, M. R. Tonks, Rapid multiphase-field model development using a modular free energy based approach with automatic differentiation in moose/marmot, Computational Materials Science 132 (2017) 36–45.

[8] M. Song, M. Wang, X. Lou, R. B. Rebak, G. S. Was, Radiation damage and irradiation-assisted stress corrosion cracking of additively manufactured 316l stainless steels, Journal of Nuclear Materials 513 (2019) 33–44.

[9] T. Byun, B. E. Garrison, M. R. McAlister, X. Chen, M. N. Gussev, T. G. Lach, A. Le Coq, K. Linton, C. B. Joslin, J. K. Carver, et al., Mechanical behavior of additively manufactured and wrought 316l stainless steels before and after neutron irradiation, Journal of Nuclear Materials 548 (2021) 152849.

[10] S. Li, J. Hu, W.-Y. Chen, J. Yu, M. Li, Y. Wang, Evolution of cellular dislocation structures and defects in additively manufactured austenitic stainless steel under ion irradiation, Scripta Materialia 178 (2020) 245–250.

[11] Z. Shang, C. Fan, J. Ding, S. Xue, A. Gabriel, L. Shao, T. Voisin, Y. M. Wang, T. Niu, J. Li, et al., Heavy ion irradiation response of an additively manufactured 316ln stainless steel, Journal of Nuclear Materials 546 (2021) 152745.

[12] B. Alexandreanu, X. Zhang, Y. Chen, W.-Y. Chen, M. Li, Mechanical testing of additively manufactured materials, Tech. Rep. ANL/NSE-22/83, Argonne National Laboratory, Argonne, Illinois (2022).

[13] M. Li, W.-Y. Chen, P. M. Baldo, In situ transmission electron microscopy with dual ion beam irradiation and implantation, Materials Characterization 173 (2021) 110905.

[14] Y. M. Wang, T. Voisin, J. T. McKeown, J. Ye, N. P. Calta, Z. Li, Z. Zeng, Y. Zhang, W. Chen, T. T. Roehling, et al., Additively manufactured hierarchical stainless steels with high strength and ductility, Nature materials 17 (1) (2018) 63–71.

[15] M. Li, M. Kirk, P. Baldo, D. Xu, B. Wirth, Study of defect evolution by tem with in situ ion irradiation and coordinated modeling, Philosophical Magazine 92 (16) (2012) 2048–2078.

[16] W.-Y. Chen, M. Li, Tem study of nickel under in-situ helium/krypton dual-beam irradiation, in: Transactions of the American Nuclear Society, Volume 120, American Nuclear Society, 2019, p. 339.

[17] M. Li, X. Zhang, W.-Y. Chen, T. S. Byun, Creep behavior of 316 l stainless steel manufactured by laser powder bed fusion, Journal of Nuclear Materials 548 (2021) 152847.

[18] M. L. Waskom, Seaborn: statistical data visualization, Journal of Open Source Software 6 (60) (2021) 3021.

[19] J. Piochaud, M. Nastar, F. Soisson, L. Thuinet, A. Legris, Atomic-based phase-field method for the modeling of radiation induced segregation in fe–cr, Computational Materials Science 122 (2016) 249–262.

[20] J. R. Manning, Cross terms in the thermodynamic diffusion equations for multicomponent alloys, Metallurgical and Materials Transactions B 1 (1970) 499–505.

[21] Y. Yang, K. G. Field, T. R. Allen, J. T. Busby, Roles of vacancy/interstitial diffusion and segregation in the microchemistry at grain boundaries of irradiated fe–cr–ni alloys, Journal of nuclear materials 473 (2016) 35–53.

[22] H. Wiedersich, P. Okamoto, N. Q. Lam, A theory of radiation-induced segregation in concentrated alloys, Journal of Nuclear Materials 83 (1) (1979) 98–108.

[23] M. Norgett, M. Robinson, I. M. Torrens, A proposed method of calculating displacement dose rates, Nuclear engineering and design 33 (1) (1975) 50–54.

[24] L. Xia, Y. Ji, W. Liu, H. Chen, Z. Yang, C. Zhang, L.-Q. Chen, Radiation induced grain boundary segregation in ferritic/martensitic steels, Nuclear Engineering and Technology 52 (1) (2020) 148–154.

[25] K. G. Field, Y. Yang, T. R. Allen, J. T. Busby, Defect sink characteristics of specific grain boundary types in 304 stainless steels under high dose neutron environments, Acta Materialia 89 (2015) 438–449.

[26] G. Was, P. Andresen, Stress corrosion cracking behavior of alloys in aggressive nuclear reactor core environments, Corrosion 63 (1) (2007) 19–45.

[27] L. Thuinet, H. Rouchette, A. Legris, 3d phase-field modelling of dislocation loop sink strengths, Journal of Nuclear Materials 483 (2017) 62–81.

[28] N. Moelans, A quantitative and thermodynamically consistent phase-field interpolation function for multi-phase systems, Acta Materialia 59 (3) (2011) 1077–1086.

[29] N. Moelans, B. Blanpain, P. Wollants, Quantitative analysis of grain boundary properties in a generalized phase field model for grain growth in anisotropic systems, Physical Review B 78 (2) (2008) 024113.

[30] T. Klaver, D. Hepburn, G. Ackland, Defect and solute properties in dilute fe-cr-ni austenitic alloys from first principles, Physical Review B 85 (17) (2012) 174111.

[31] J. Piochaud, T. Klaver, G. Adjanor, P. Olsson, C. Domain, C. Becquart, First-principles study of point defects in an fcc fe-10ni-20cr model alloy, Physical review B 89 (2) (2014) 024101.

[32] M. J. Hackett, J. T. Busby, G. Was, The mechanism of zr and hf in reducing radiation-induced segregation in 316 stainless steel, Metallurgical and Materials Transactions A 39 (2008) 218–224.

[33] T. Allen, G. Was, Modeling radiation-induced segregation in austenitic fe–cr–ni alloys, Acta materialia 46 (10) (1998) 3679–3691.

[34] J. R. Manning, Correlation factors for diffusion in nondilute alloys, Physical Review B 4 (4) (1971) 1111.

[35] J. Miettinen, Thermodynamic reassessment of fe-cr-ni system with emphasis on the iron-rich corner, Calphad 23 (2) (1999) 231–248.

[36] G. Ghosh, G. Olson, The isotropic shear modulus of multicomponent fe-base solid solutions, Acta materialia 50 (10) (2002) 2655–2675.

[37] R. Stoller, Modeling dislocation evolution in irradiated alloys, Metallurgical Transactions A 21 (1990) 1829–1837.

[38] S. Watanabe, Y. Takamatsu, N. Sakaguchi, H. Takahashi, Sink effect of grain boundary on radiation-induced segregation in austenitic stainless steel, Journal of nuclear materials 283 (2000) 152–156.

[39] R. Skorokhod, A. Koropov, Modeling of radiation-induced segregation in fe–cr–ni alloys, Physics of the Solid State 61 (2019) 2269–2276.

[40] C. Li, F. Chen, G. Ge, J. Lin, Z. Sun, M. Fan, P. Huang, X. Tang, Impact of sub-grain structure on radiation resistance in additively manufactured 316l stainless steels: An atomic insight into the mechanism, Applied Surface Science 606 (2022) 154926.

[41] S. Zinkle, P. Maziasz, R. Stoller, Dose dependence of the microstructural evolution in neutron-irradiated austenitic stainless steel, Journal of Nuclear materials 206 (2-3) (1993) 266–286.

[42] M. Mamivand, Y. Yang, J. Busby, D. Morgan, Integrated modeling of second phase precipitation in cold-worked 316 stainless steels under irradiation, Acta Materialia 130 (2017) 94–110.

[43] A. P. Thompson, H. M. Aktulga, R. Berger, D. S. Bolintineanu, W. M. Brown, P. S. Crozier, P. J. in 't Veld, A. Kohlmeyer, S. G. Moore, T. D. Nguyen, R. Shan, M. J. Stevens, J. Tranchida, C. Trott, S. J. Plimpton, LAMMPS - a flexible simulation tool for particle-based materials modeling at the atomic, meso, and continuum scales, Comp. Phys. Comm. 271 (2022) 108171. doi:10.1016/j.cpc.2021.108171.

[44] M. S. Daw, M. I. Baskes, Embedded-atom method: Derivation and application to impurities, surfaces, and other defects in metals, Phys. Rev. B 29 (1984) 6443–6453. doi:10.1103/PhysRevB.29.6443.
URL https://link.aps.org/doi/10.1103/PhysRevB.29.6443

[45] J. Tersoff, New empirical approach for the structure and energy of covalent systems, Phys. Rev. B 37 (1988) 6991–7000. doi:10.1103/PhysRevB.37.6991.
URL https://link.aps.org/doi/10.1103/PhysRevB.37.6991

[46] X. W. Zhou, M. E. Foster, R. B. Sills, An fe-ni-cr embedded atom method potential for austenitic and ferritic systems, Journal of Computational Chemistry 39 (29) (2018) 2420–2431. arXiv:https://onlinelibrary.wiley.com/doi/pdf/10.1002/jcc.25573, doi:https://doi.org/10.1002/jcc.25573.
URL https://onlinelibrary.wiley.com/doi/abs/10.1002/jcc.25573

[47] L. K. Béland, A. Tamm, S. Mu, G. Samolyuk, Y. Osetsky, A. Aabloo, M. Klintenberg, A. Caro, R. Stoller, Accurate classical short-range forces for the study of collision cascades in fe–ni–cr, Computer Physics Communications 219 (2017) 11–19. doi:https://doi.org/10.1016/j.cpc.2017.05.001.
URL https://www.sciencedirect.com/science/article/pii/S0010465517301315

[48] K. O. E. Henriksson, C. Björkas, K. Nordlund, Atomistic simulations of stainless steels: a many-body potential for the fe–cr–c system, Journal of Physics: Condensed Matter 25 (44) (2013) 445401. doi:10.1088/0953-8984/25/44/445401.
URL https://dx.doi.org/10.1088/0953-8984/25/44/445401

[49] J. Ziegler, J. Biersack, M. Ziegler, SRIM, the Stopping and Range of Ions in Matter, SRIM Company, 2008.
URL https://books.google.com/books?id=JSN63qxPG5MC

[50] K. Nordlund, Molecular dynamics simulation of ion ranges in the 1–100 kev energy range, Computational Materials Science 3 (4) (1995) 448–456. doi:https://doi.org/10.1016/0927-0256(94)00085-Q.
URL https://www.sciencedirect.com/science/article/pii/092702569400085Q

[51] K. Nordlund, M. Ghaly, R. S. Averback, M. Caturla, T. Diaz de la Rubia, J. Tarus, Defect production in collision cascades in elemental semiconductors and fcc metals, Phys. Rev. B 57 (1998) 7556–7570. doi:10.1103/PhysRevB.57.7556.
URL https://link.aps.org/doi/10.1103/PhysRevB.57.7556

[52] J. P. Biersack, J. F. Ziegler, The stopping and range of ions in solids, in: H. Ryssel, H. Glawischnig (Eds.), Ion Implantation Techniques, Springer Berlin Heidelberg, Berlin, Heidelberg, 1982, pp. 122–156.

[53] S. Nosé, A unified formulation of the constant temperature molecular dynamics methods, The Journal of Chemical Physics 81 (1) (1984) 511–519. arXiv:https://pubs.aip.org/aip/jcp/article-pdf/81/1/511/9722086/511_1_online.pdf, doi:10.1063/1.447334.
URL https://doi.org/10.1063/1.447334

[54] W. G. Hoover, Canonical dynamics: Equilibrium phase-space distributions, Phys. Rev. A 31 (1985) 1695–1697. doi:10.1103/PhysRevA.31.1695.
URL https://link.aps.org/doi/10.1103/PhysRevA.31.1695

[55] A. Stukowski, Visualization and analysis of atomistic simulation data with ovito–the open visualization tool, Modelling and Simulation in Materials Science and Engineering 18 (1) (2009) 015012. doi:10.1088/0965-0393/18/1/015012.
URL https://dx.doi.org/10.1088/0965-0393/18/1/015012

[56] Y. Yang, K. G. Field, T. R. Allen, J. T. Busby, Roles of vacancy/interstitial diffusion and segregation in the microchemistry at grain boundaries of irradiated fe–cr–ni alloys, Journal of Nuclear Materials 473 (2016) 35–53. doi:https://doi.org/10.1016/j.jnucmat.2016.02.007.
URL https://www.sciencedirect.com/science/article/pii/S0022311516300605

[57] R. Stoller, 1.11-primary radiation damage formation, Comprehensive nuclear materials (2012) 293–332.

[58] N. Anento, A. Serra, Carbon–vacancy complexes as traps for self-interstitial clusters in fe–c alloys, Journal of Nuclear Materials 440 (1-3) (2013) 236–242.

[59] C. J. Först, J. Slycke, K. J. Van Vliet, S. Yip, Point defect concentrations in metastable fe-c alloys, Physical review letters 96 (17) (2006) 175501.

[60] W.-Y. Chen, Y. Miao, Y. Wu, C. A. Tomchik, K. Mo, J. Gan, M. A. Okuniewski, S. A. Maloy, J. F. Stubbins, Atom probe study of irradiation-enhanced α' precipitation in neutron-irradiated fe–cr model alloys, Journal of Nuclear Materials 462 (2015) 242–249. doi:https://doi.org/10.1016/j.jnucmat.2015.04.005.
URL https://www.sciencedirect.com/science/article/pii/S0022311515002068